Anomalous Pressure Diffusion in Heterogeneous Porous Media – Final Report submitted to Nederlandse Aardolie Maatschappij (NAM)

Authors: Prof Sebastian Geiger, Prof Gabriel Lord, Dr Robert Annewandter, Heriot-Watt University, Edinburgh, United Kingdom

Date: June 22, 2015

1   Executive Summary

We present results from 360 high-resolution numerical simulations in 2D and 240 high-resolution simulations in 3D that investigate under which circumstances anomalous pressure diffusion could occur in heterogeneous geological formations. To mimic geological heterogeneity, we have generated multiple realisations of random fields in 2D and 3D with varying degrees of heterogeneity. We used fractional Brownian motion (in 2D) and exponential covariances (in 2D and 3D) to generate the random fields. Breakthrough curves of normalised pressure vs. normalised time were recorded in the numerical simulations. These breakthrough curves often show early breakthrough and late-time tailing if there is sufficient heterogeneity in the random fields; both are strong evidence of anomalous pressure diffusion. Early breakthrough and late-time tailing in the breakthrough curves are generated by areas in the model where the pressure diffuses significantly faster, respectively significantly slower, compared to model predictions that assume a uniform hydraulic diffusivity that is equal to the mean of the random field. These regions could possibly correspond to areas where the reservoir compacts faster or slower than what would be expected from traditional reservoir simulations that employ average permeabilities at the scale of a reservoir simulation grid-block.

2   Anomalous Diffusion

2.1   Principles and Characteristics

The transport of particles and heat during single-phase miscible flow is commonly described by an advection-dispersion equation

$$\frac{\partial \alpha(\boldsymbol{x})}{\partial t} + \nabla \cdot \big(\boldsymbol{v}(\boldsymbol{x})\boldsymbol{\alpha}(\boldsymbol{x}) + \eta(\boldsymbol{x})\nabla\alpha(\boldsymbol{x})\big) = 0 \text{ with } \alpha \in \{c, T\}, \tag{1}$$

where α is the transported quantity (e.g. concentration c or temperature T, $\boldsymbol{v}$ is the Darcy velocity, η the diffusion coefficient and $\boldsymbol{x}$ a vector of spatial coordinates. Note that Equation (1) reduced to the diffusivity equation if $\boldsymbol{v}(\boldsymbol{x}) = 0$ and $\alpha = p$

$$\frac{\partial p(\boldsymbol{x})}{\partial t} + \nabla \cdot \big(\eta(\boldsymbol{x})\nabla p(\boldsymbol{x})\big) = 0 \text{ with } \eta = \frac{k}{\mu c_t}. \tag{2}$$

Equation (1) predicts that the first spatial moment is proportional to time, i.e. distance l that the peak of α has moved along the velocity field $\boldsymbol{v(x)}$ is $l(t) \propto t$. Similarly, the second spatial moment, i.e. the rate at which the peak of α decays and the variance σ of α grows due to diffusion, has the relation $\sigma(t) \propto \sqrt{t}$ (Figure 1).

However, it has been widely observed that transport in (even relatively homogeneous) geological formations does not follow the behaviour described in Equation (1) and illustrated Figure 1. Instead, it is normally characterised by long tails (slow breakthrough) and fast leading edges (early breakthrough) (Figure 2). Hence the first and second spatial moments exhibit a scaling that is very different from t and $\sqrt{t}$, respectively. This type of behaviour is normally described as anomalous diffusion or transport and also known as non-Fickian transport and indeed appears to be the "normal" transport behaviour in geological formations (c.f. Berkowitz et al. 2006).
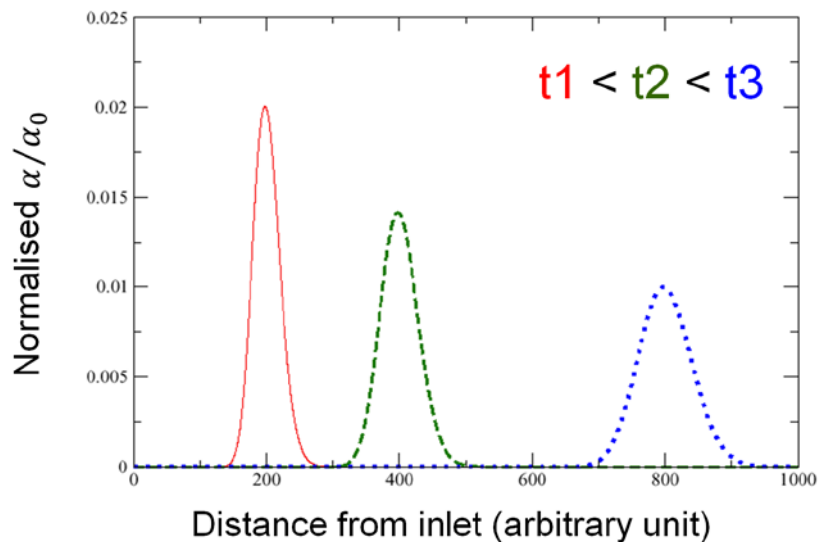

Figure 1. Spatial profiles of a concentration plume at three different times (t1, t2, t3). The plume travels from left to right in a 1D porous media due to advection and diffusion. Transport is assumed to be of classical (Fickian) nature, i.e. can be described macroscopically by Equation (1). Note that the centre of the plume (peak of α) moves proportional to time t, that the peak of α decays proprotial to $\sqrt{t}$ and the variance of the plume grows proportional to $\sqrt{t}$. Adapted from Berkowitz et al. (2006).
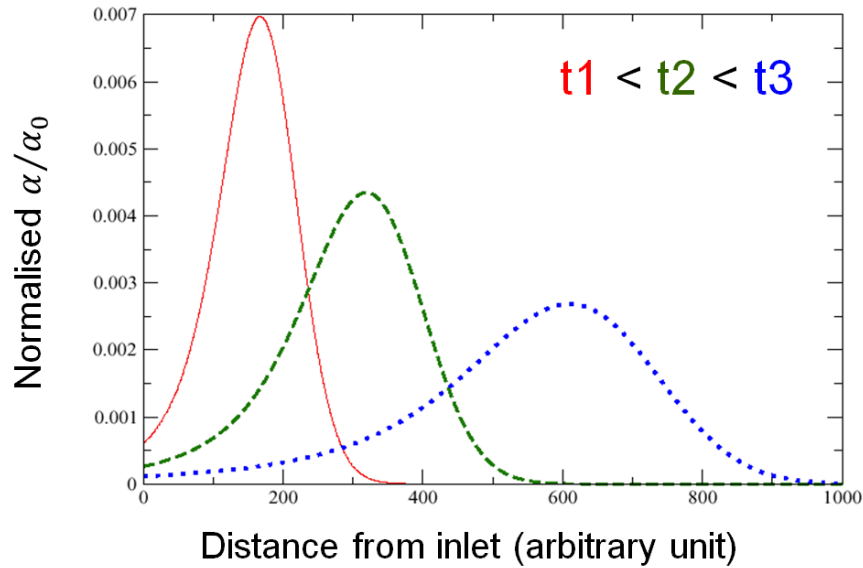
Figure 2. Spatial profiles of a concentration plume at three different times (t1, t2, t3). The plume travels from left to right in a 1D porous media due to advection and diffusion. Transport is assumed to be of anomalous (non-Fickian) nature, i.e. cannot be described macroscopically by Equation (1). Note that, compared to Figure 1, the centre of the plume (i.e. peak of α) moves no longer proportional to time t, the peak of α decays no longer proportionally to $\sqrt{t}$, and the variance of the plume grows no longer proportionally to $\sqrt{t}$. Instead, one can observe fast leading edges in the concentration plumes and long tails, i.e. fast breakthrough and slow breakthrough, respectively. Figure modified from Berkowitz et al. (2006).

Anomalous transport is widely observed for single-phase miscible flow, from the pore- to the reservoir scale and in both, fractured and unfractured geological formations (e.g., Di Donato et al., 2003; Cortis and Berkowitz, 2004; Cortis et al., 2004; Bijeljic and Blunt, 2006; Geiger et al., 2010). An interesting observation in anomalous diffusion is that small-scale heterogeneities do not average out at larger scales (Rhodes et al., 2009). Instead, small-scale (core, plug, outcrop) heterogeneities accumulate to yield anomalous transport at the large (e.g. reservoir scale). However, anomalous transport transitions to normal (Fickian) transport at sufficiently long times-scales, that is if transport has experienced, on average, all of the heterogeneity of the geological formation (Dentz et al., 2004).

While anomalous diffusion is common in solute transport processes and has been also observed for heat transport (Geiger and Emmanuel, 2010) and pressure diffusion (Cortis and Knudby, 2006; see Figure 3), it is less common for the latter two applications. This is because solute transport is dominated by advective processes while diffusive processes dominate heat transport and pressure diffusion. Hence solute, heat transport, and pressure diffusion average at different time- and length-scales, i.e. the transition to normal diffusion occurs at significantly shorter time- and length-scales for heat transport and pressure diffusion compared to solute transport. Hence anomalous diffusion appears to be less common during heat transport and pressure diffusion.
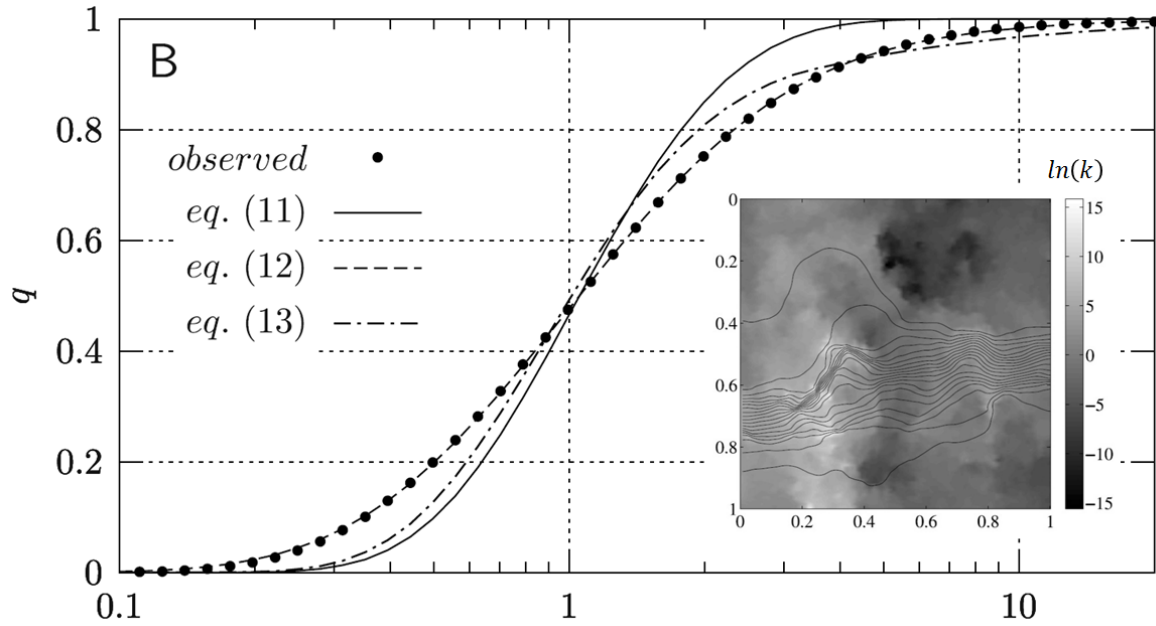
Figure 3. Example of anomalous pressure diffusion in a 2D geological domain. The inset shows the heterogeneity in the permeability field. A numerical simulation models the movement of a pressure front from left to right through this permeability field. The average and normalised flow velocity q is monitored at the right model boundary. Initially q is zero as the pressure gradient at the right model boundary is zero. q then increases with time as the pressure front reaches the model boundary. The numerically generated data (denoted as "observed" in the figure legend) shows clear indication of early breakthrough and tailing that cannot be captured by classical diffusion and Equation (1) (denoted as eq. 11 in the figure legend). The more general Continuous Time Random Walk (CTRW) approach, however, enables us to capture anomalous pressure diffusion by resolving the full spectrum of transition times which can be modelled through a truncated power-law (denoted as eq. 12 in the figure legend) or a modified exponential (denoted as eq. 13 in the figure legend). See Section 2.2 for a discussion of CTRW. Figure modified from Cortis and Knudby (2006).

2.2 Mathematical Models for Anomalous Transport

A number of mathematical approaches have been developed to model anomalous transport, including but not limited to fractional advection dispersion equations (Benson et al., 2000), multi-rate mass transfer models (Haggerty and Gorelick, 1995), or continuous time random walks (Berkowitz et al., 2006). However, it has now been suggested that the former two approaches are special cases of the more general continuous time random walk (CTRW) approach (Berkowitz et al., 2006).

The central idea of the CTRW is not to describe macroscopic transport at the reservoir or grid-block scale by the averaged parameters inherent to Equation (1) but to capture the full spectrum of transition times inherent to the geological formation, i.e. the time it takes for the dissolved particles in a concentration plume to migrate through a geological formation. Short transition times correspond to regions in the reservoir where flow is fast while long transition times correspond to regions where flow is slow or stagnant.

CTRW is the general form of a random walk and encapsulates a distribution of transition times $\psi(t)$ that quantifies the distribution of time-steps Δt that a particle needs to move a certain distance x through the geological formation. Long time-steps (i.e. large transition times) are encountered when the particle travels through low-permeability regions while short time-steps (i.e. short transition times) are encountered when the particle travels through high-permeability regions.

When accounting for the full spectrum of transition times $\psi(t)$ in a mathematical model such as CTRW, the statistically rate fast and/or slow events that lead to early breakthrough and long tails, and subsequently to anomalous diffusion, are intrinsically captured. It should be noted, however, that anomalous transport would always emerge if we were able to simulate flow and transport in a geological formation using grids that have centimetre-scale (or even higher) resolution. Such grids would resolve all small-scale heterogeneities and the fast/slow transport of particles through them, i.e. capture the statistically rate fast and/or slow events that lead to anomalous diffusion.

The CTRW equivalent of Equation (1) in Laplace space is given by

$$u\tilde{\alpha}(\boldsymbol{s}, u) - \alpha_0(\boldsymbol{s}) = -\tilde{M}(u)[\boldsymbol{v} \cdot \nabla\tilde{\alpha}(\boldsymbol{s}, u) + \eta\nabla^2\tilde{\alpha}(\boldsymbol{s}, u)], \qquad (3)$$

where the tilde indicates a property in Laplace space, u is equivalent to time in Laplace space and $\boldsymbol{s}$ to $\boldsymbol{x}$ in Laplace space. $\tilde{M}(u)$ is a memory function that encapsulates the distribution of transition times transition times $\psi(t)$.
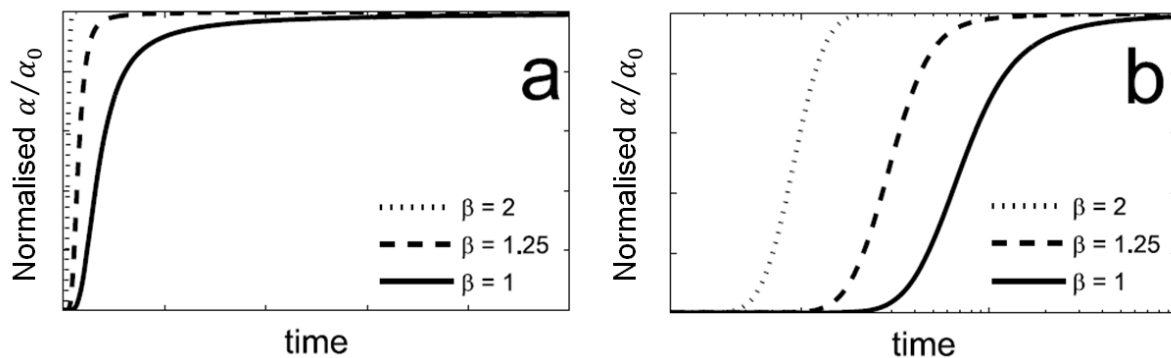

Figure 4. Breakthrough curves (α vs. t) showing the relationship between β and anomalous diffusion for linear time (a) and log10 time (b). Anomalous diffusion emerges if $0 \leq \beta \leq 2$ and the smaller β, the more anomalous diffusion becomes, i.e. the more tailing at late time and early breakthrough can be observed in the breakthrough curves. Modified from Geiger and Emmanuel (2010).

For anomalous diffusion, it was demonstrated that $\psi(t)$ can be readily modelled by a truncated power-law for a wide range of geological formations (cf. Berkowitz et al., 2006). The truncated power-law contains three parameters, the most important one being an exponent β that indicates the heterogeneity of the geological formation and relates to $\psi(t)$ as $\psi(t) \sim t^{-1-\beta}$. For values of β between $0 \leq \beta \leq 2$, diffusion is anomalous and generally, the smaller β, the more anomalous diffusion is (Figure 4).

Using CTRW with a truncated power-law to model $\psi(t)$ enables the straightforward detection and robust quantification of anomalous diffusion in breakthrough curves by fitting the parameters of the truncated power-law, most notably β, to the experimentally or numerically derived breakthrough curves. If $\beta < 2$, diffusion is anomalous. The relevant fitting routines are available in the CTRW Toolbox (Cortis and Berkowitz, 2005).

3 Random Field Generation

In order to test if and when pressure diffusion can be anomalous, we solve Equation (2) on 2D and 3D domains where the hydraulic diffusivity $\eta(x)$ is randomly distributed. To achieve this we generate random fields $u(x)$ with $x \in R^2$ (2D) or $x \in R^3$ (3D) and then exponentiate. Hence we compute with $v(x) = \exp(u(x))$ which ensures that $\eta(x)$ is always positive. We note that the resulting random fields are purely synthetic and not related to a particular subsurface reservoir, as discussed in the meeting in Assen on May 1, 2015.

We characterise the random field $u(x)$ with a covariance $C(x, y)$ given by

$$C(x, y) = \text{Cov}(u(x), u(y)) = E[(u(x) - E[u(x)])(u(y) - E[u(y)])^T]. \qquad (4)$$

$u(x)$ is said to be a stationary random field if it is invariant to translations, the mean is constant, so that $E(u(x)) = \mu$ and $C(x, y) = c(x - y)$. $u(x)$ is said to be isotropic if it is invariant to rotations, that is the covariance function is stationary and $c(x) = c(r)$, where $r = \|x\|$. Essentially the random field looks (on average) the same in every direction with no special features built in. Thus, any anomalous diffusion has not been inserted, from the choice of features in the random field.

In particular we consider two types of isotropic fields:

1. An exponential covariance where the covariance function satisfies $c(r) = \exp(-r/\ell)$ for a given correlation length-scale ℓ for both, $x \in R^2$ and $x \in R^3$. We take $\ell = 0.1, 0.01,$ and 0.001 on the domain $[0,1] \times [0,1]$ and $\ell = 0.1$ and 0.01 on the domain $[0,1] \times [0,1] \times [0,1]$. This ensures we can resolve the length-scales over which heterogeneity occurs with our spatial discretisation.

2. A Fractional Brownian field with covariance $E\left(B^{\mathcal{H}}(t)B^{\mathcal{H}}(s)\right) = 0.5\left(\|t\|^{2\mathcal{H}} + \|s\|^{2\mathcal{H}} - \|t - s\|^{\mathcal{H}}\right)$. The parameter $\mathcal{H}$ determines the smoothness of the field. With $\mathcal{H} = 0.5$ the field is a Brownian field (and 1D increments are independent). For $\mathcal{H} > 0.5$ increments are positively correlated and for $\mathcal{H} < 0.5$ negatively correlated. We consider $\mathcal{H} = 0.25, 0.5$ and 0.75.

Random fields with exponential covariance are approximated by using a Turning Bands approach. This idea is based on a sequence of 1D simulations and the central limit theorem (Montogolou and Wilson, 1982; Gneiting, 1998; Lord et al., 2014) and is an effective method for producing fields in 3D. The fractional Brownian field is constructed using a circulent embedding approach which is better suited to 2D problems (Dietrich and Newsam, 1997; Lord et al., 2014; Kroese and Botev, 2014).
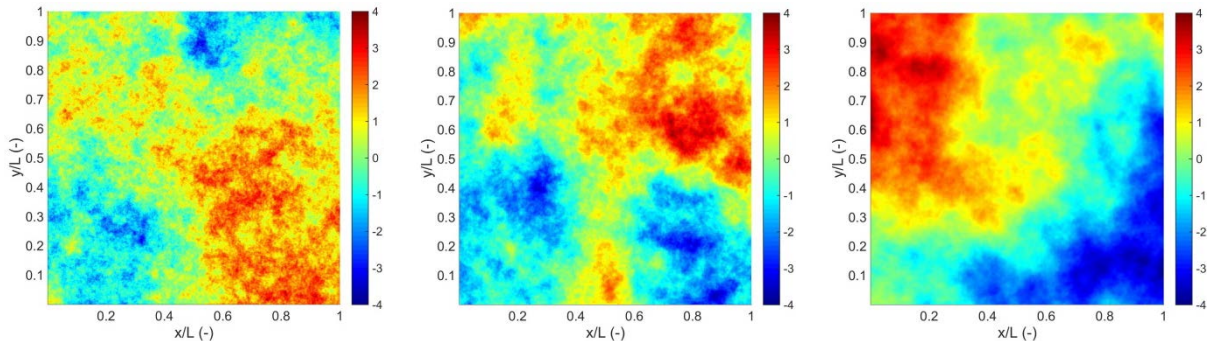

Figure 5. Exemplary random fields with $x \in R^2$ for fractional Brownian motion with $\log_{10}(\eta) \in [-4, 4]$ and $\mathcal{H} = 0.25, 0.5$ and 0.75 (from left to right).
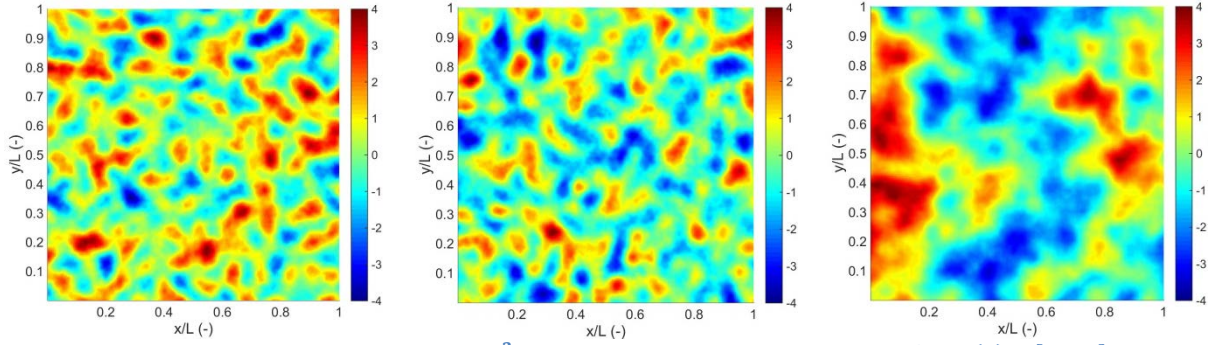
Figure 6. Exemplary random fields with $x \in R^2$ for an exponential covariance with $\log_{10}(\eta) \in [-4, 4]$ and $\ell = 0.001, 0.01$ and 0.1 (from left to right).
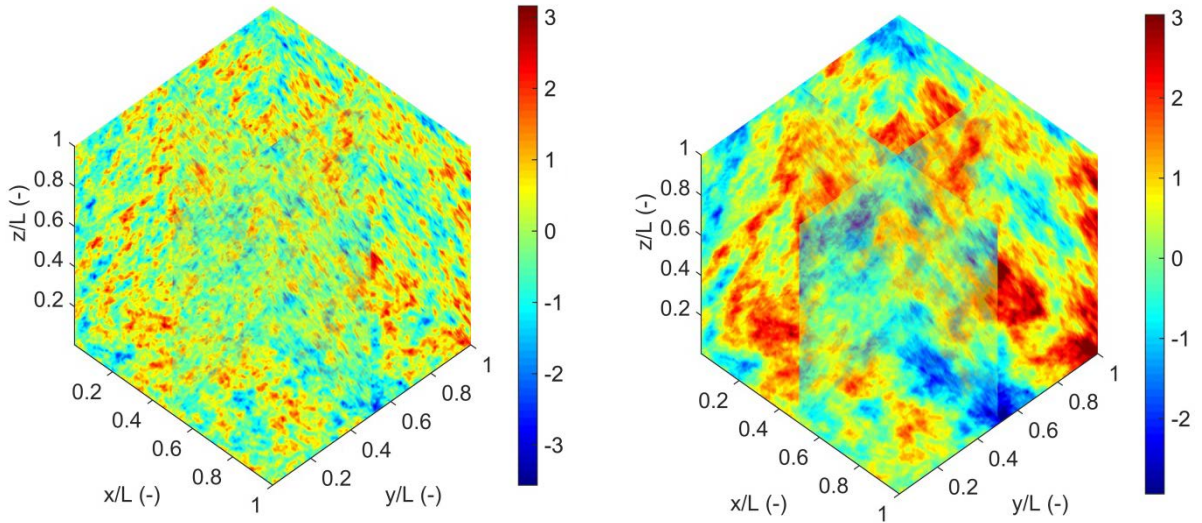

Figure 7. Two-dimensional cross-sections through exemplary random fields with $x \in R^3$ for an exponential covariance with $\log_{10}(\eta) \in [-4, 4]$ and $\ell = 0.01$ and 0.1 (from left to right).

The random fields $u(x)$ were generated using these two techniques and then rescaled to set the maximum and minimum values in the field and hence variation in $\eta(x)$. We consider variations in $\log_{10}(\eta)$ between $[-2,2]$, $[-4,4]$ and $[-6,6]$ for both 2D and 3D. For all fields we set the mean of $\log_{10}(\eta) = 0$. We generated ten different realisations for each combination of $[\eta_{\min}, \eta_{\max}]$ and ℓ (for the exponential covariance), respectively $\mathcal{H}$ (for the fractional Brownian fields). Hence in total we obtained 90 random fields in 2D using an exponential covariance, 90 random fields in 2D using fractional Brownian motion, and two sets of 60 random fields in 3D using an exponential covariance, one for a grid of $100 \times 100 \times 100$ and one for a grid of $200 \times 200 \times 200$ to test the impact of grid refinement on anomalous diffusion in 3D. Simulations were carried out for all fields with two different set of boundary conditions (see below). Exemplary random fields are shown in Figure 5 (fractional Brownian motion in 2D), Figure 6 (exponential covariance in 2D) and Figure 7 (exponential covariance in 3D).

4   Numerical Simulations

4.1   Discretisation of Governing Equations and Simulation Setup

We used our in-house simulation software CSMP++ (Matthäi et al., 2007) to solve Equation (2) numerically with a standard Galerkin finite element method. The 2D domains were hence discretised by uniform quadrilateral finite elements, the 3D domains by uniform hexahedral finite elements. An

algebraic multigrid solver (Stüben, 2007) was used for the efficient inversion of the resulting linear system, providing optimal, i.e. $n\log(n)$, scaling.

The 2D domain was a square with dimensions $[L \times L]$. It was discretised by 1000×1000 finite elements. The 3D domain was a square with dimensions $[L \times L \times L]$. It was discretised by $100 \times 100 \times 100$ finite elements and $200 \times 200 \times 200$ to test the impact of grid refinement on anomalous diffusion in 3D. Random fields were generated at the same resolution as the simulation grid, using the methods discussed in Section 3 above for the exponential covariance and fractional Brownian motion.
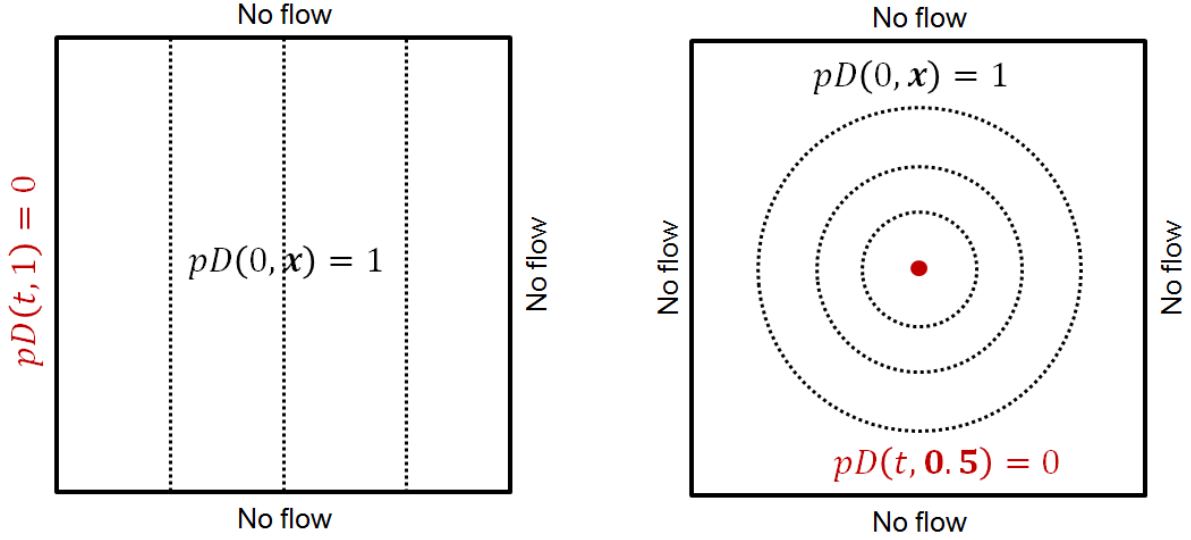

Figure 8. Simulation setup showing initial and boundary conditions in 2D. Note that the same initial and boundary conditions are applied in 3D. Left: Diffusion from left to right due to a fixed pressure drop that is applied along the entire left model boundary (for both, 2D and 3D). Right: Radial diffusion towards due to a fixed pressure drop located at a single point located in the centre of the model (for both, 2D and 3D). Initially, the normalised reservoir pressure $pD(0,x)$ is set to 1 everywhere in the domain. Note that all model boundaries in the radial diffusion scenario are no-flow boundaries. In the left-to-right diffusion scenario, all model boundaries with exception of the boundary where the pressure drop is applied were no-flow boundaries. The dashed lines denote lines (in 2D) and surfaces (in 3D) where the average pressure is recorded as a function of time. For the left-to-right diffusion simulations, they are located at a non-dimensional distance $\xi = x/L \in [0.25, 0.5, 0.75]$. For the radial diffusion simulations, they are located at a non-dimensional radial distance $\rho = r/R \in [0.25, 0.5, 0.75]$. Note that L is the total length of the model and the same in the x, y and z-direction. In other words, the 2D domains are squares and the 3D domains cubes and the average pressure is always recorded as a function of time at one quarter, one half, and three quarters away from the location where the pressure is initially perturbed.

Implicit time-stepping was used in all simulations. The initial time-step was set to $\Delta t = 10^{-4} tD$ where tD is the non-dimensional time defined as $tD = \eta t/d^2$ where t is time and d is the distance between the location where the pressure is perturbed and the nearest reservoir boundary. The Δt then increased by 10% during each time-step to find a good compromise between computational efficiency and resolving the early-time behaviour appropriately, i.e. when pressure gradients are steep and change rapidly.

The initial conditions are the same for all 2D and 3D simulations and all 180 random fields in 2D and the two sets of 60 random fields with different levels of grid refinement in 3D. However, two different set of initial conditions were applied (Figure 8). The first initial condition caused a pressure wave to travel from left to right through the domain. The second initial condition caused radial

diffusion away from a single point. Both set of boundary conditions were applied to all random fields in 2D and 3D. Hence in total 360 simulations were run in 2D and 240 simulations were run in 3D.

4.2 Presentation of Results and Analysis of Anomalous Diffusion

Throughout the simulations, physically realistic values for fluid pressure, permeability, compressibility, fluid viscosity, and model domain size were used, although these are not related to a particular subsurface reservoir. However, we non-dimensionalised all variables when presenting the results. This enables us to study anomalous diffusion independently of a given time- or length-scale. In other words, the results presented below can be interpreted with respect to the length- and time-scales pertinent to a reservoir simulation grid block or an entire geological formations. To this end, we use the following non-dimensional variables:

- Non-dimensional time is $tD = \eta t / d^2$. Note that d is the distance between the nearest reservoir boundary and the location where the pressure is perturbed, i.e. $d = L$ for the case where the pressure diffuses from left to right and $d = L/2$ for the case where pressure diffuses radially towards a single point.
- Non-dimensional pressure is $pD = (p - p_{bc})/(p_0 - p_{bc})$, where p is the fluid pressure at a given grid point in the simulation model, p_{bc} is the pressure applied as a boundary condition (either along the left model boundary for the left-to-right diffusion case or at the central point in the model domain for the radial diffusion case), and p_0 is the fluid pressure in the reservoir at $t = 0$.
- Non-dimensional distance is $\xi = x/L$ and non-dimensional radius is $\rho = r/R$ with $R = L/2$.

While surface plots showing the distribution of pD in the model domain at different times are highly informative and will be presented below, the key property to assess if diffusion is anomalous are breakthrough curves (see Section 2.2). We therefore recorded breakthrough curves, i.e. pD as a function of non-dimensional time tD, at three different locations in the model, for both, the left-to-right and the radial diffusion cases, in all 2D and 3D simulations. Breakthrough curves for pD for the diffusion from left to right were recorded along lines (in 2D) and surfaces (in 3D) for normalised distances $\xi = x/L \in [0.25, 0.5, 0.75]$ away from the right of the left model boundary (Figure 8). For the radial diffusion simulations, breakthrough curves were recorded along lines (in 2D) and surfaces (in 3D) located at non-dimensional radial distances $\rho = r/R \in [0.25, 0.5, 0.75]$ away from the centre point (Figure 8). The average $\widehat{pD}(t)$ was measured for each time-step for each node i that is located along these lines/surfaces as $\widehat{pD}(t) = \sum pD_i(t)/N$ where N is the total number of nodes at the given line/surface.

An exemplary breakthrough curve for left-to-right diffusion case and uniform η (i.e. for classical, "normal" diffusion) is shown in Figure 9. To detect anomalous diffusion rigorously from these breakthrough curves, one would use CTRW and attempt to model the corresponding $\psi(t)$ with a truncated power-law. If the resulting parameters for the truncated power-law indicate that $0 \leq \beta \leq 2$, diffusion is anomalous.
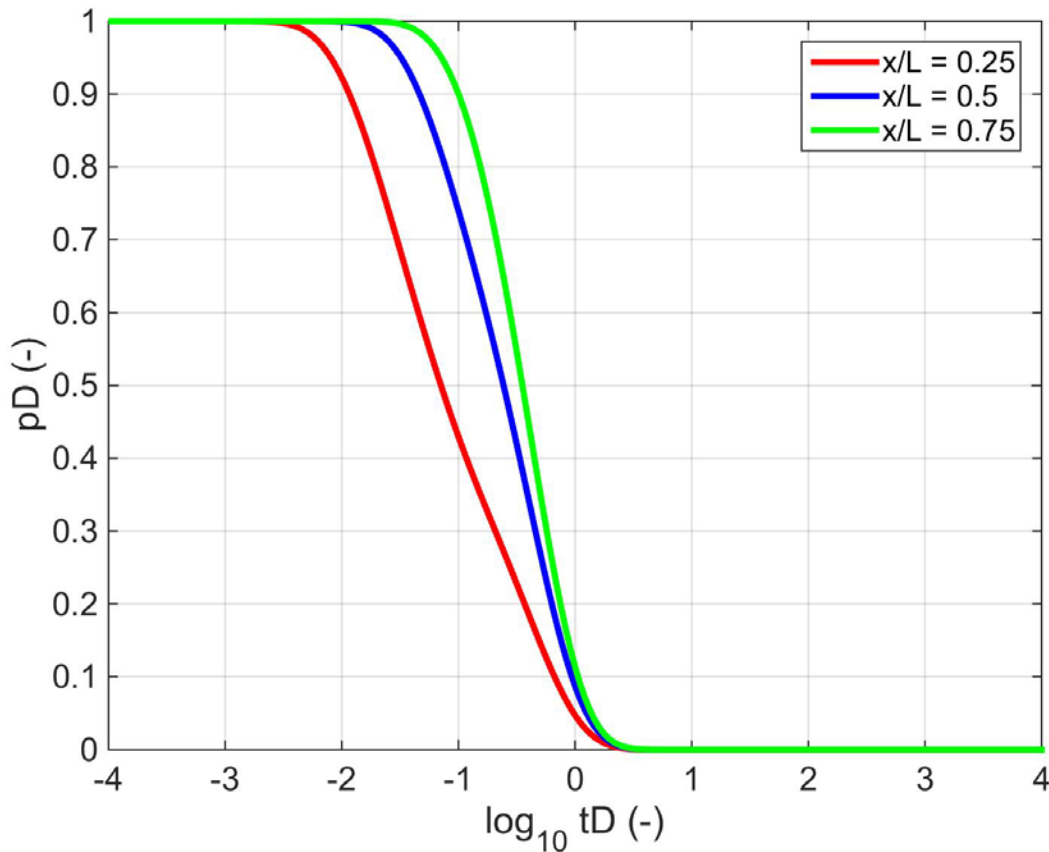
Figure 9. Exemplary breakthrough curves measured at three different distances for diffusion from left to right where η is uniform in the entire domain, i.e. for normal pressure diffusion. Deviations from these curves due to early breakthrough (i.e. pD decreases faster than average) or long tails (i.e. pD decreases slower than average) would indicate anomalous pressure diffusion. See also Figure 4 for reference.

However, as discussed in the meeting in Assen on May 1, 2015, this more rigorous quantification of anomalous diffusion is not yet followed. Hence we use the following approach to obtain semi-quantitative insights into the diffusion behaviour. We plot the resulting breakthrough curves for each of the 10 realisations for a given random field at a single normalised distance (e.g., $\xi = 0.5$) along with the breakthrough curve recorded the same distance but for a model where η is uniform and equal to the mean of the field, i.e. for $\log_{10}\eta = 0$. We then shift all breakthrough curves that we generated for the random fields such that they are centred at $pD = 0.5$ for the breakthrough curve of the uniform field. If diffusion is normal, all breakthrough curves should overlay each other. If some or all of the breakthrough curves for anomalous diffusion show early breakthrough and/or late-time tailing (which are indicative of anomalous diffusion), this is now clearly distinguishable. In addition, we count the number breakthrough curves where $pD = 0.95$ was reached *earlier* than for the breakthrough curve with the uniform $\log_{10}(\eta) = 0$ and the number of breakthrough curves where $pD = 0.05$ was reached *later* than for the breakthrough curve with the uniform $\log_{10}(\eta) = 0$. We then measure the mean ΔtD for these cases, i.e. the average difference in tD at which breakthrough occurs earlier or later than for a model where η is uniform. A large number of breakthrough curves in the ensemble that have early breakthrough and/or late-time tailing and a sufficiently large ΔtD are strong qualitative indicators, but not quantitative mathematical evidence, for anomalous diffusion. Exemplary breakthrough curves that illustrate this concept are shown in Figure 10. In the following, only the shifted breakthrough curves will be reported.
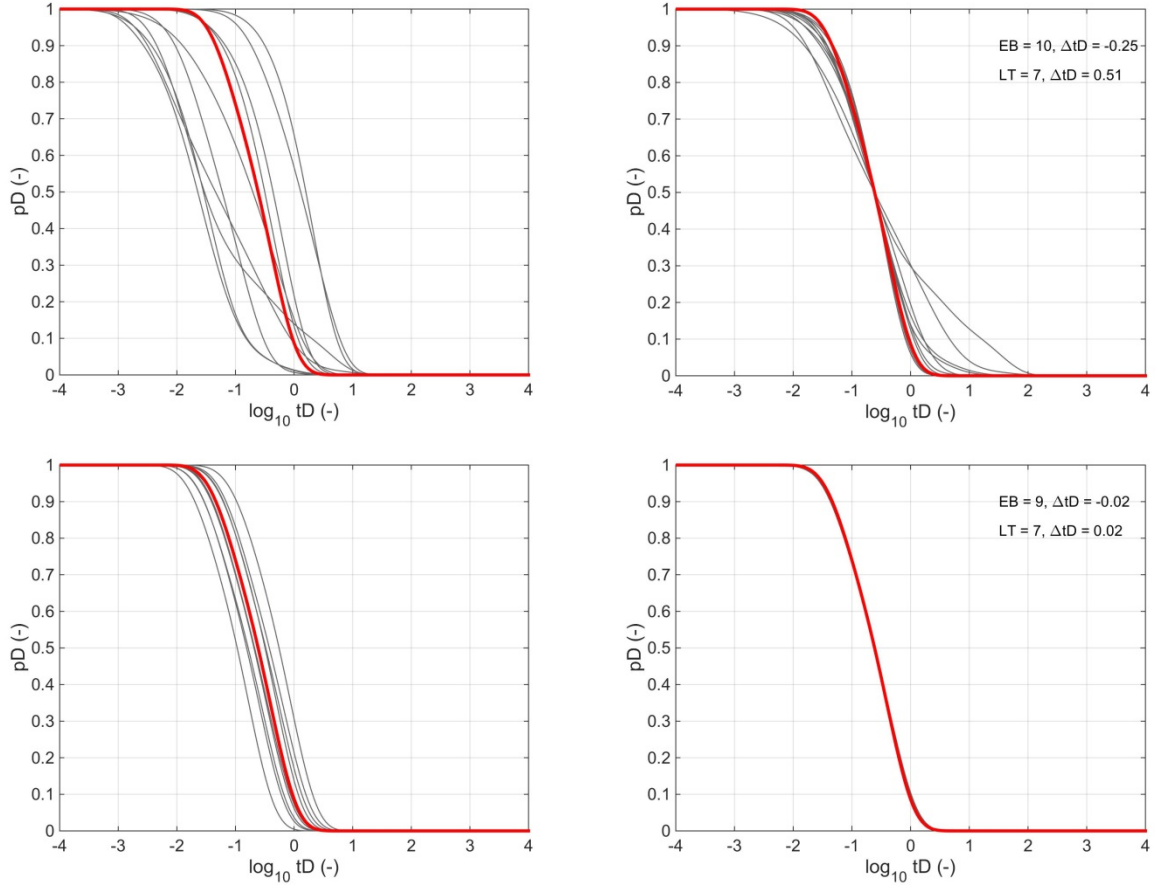
Figure 10. Examples of breakthrough curves before (left column) and after (right column) shifting, showing early breakthrough and late-time tailing, which is evidence for anomalous diffusion, (top row) and normal diffusion (bottom row). Breakthrough curves in the right column are shifted such that they centre at $pD = 0.5$. All breakthrough are recorded $\xi = 0.5$ for diffusion from left-to-right. The top row shows breakthrough curves for 2D random fields generated by fractional Brownian with $\mathcal{H} = 0.5$ and $\log_{10}(\eta) \in [-4, 4]$, the bottom row for 2D random fields that use an exponential covariance with $\ell = 0.001$ and $\log_{10}(\eta) \in [-2, 2]$. The red line indicates the breakthrough curve for a uniform field using the mean of the random field, i.e. $\log_{10}(\eta) = 0$. The grey lines are the breakthrough curves for each individual realisation of the random field. Note how all breakthrough curves for the exponential covariance fields overlay each other after shifting, which indicates that pressure diffusion is normal and can readily be modelled by the mean hydraulic diffusivity of the random field. Although 9 curves appear to show early breakthrough (EB) and 7 late-time tailing (LT) in this scenario, breakthrough is, on average, earlier by only $\log_{10}(\Delta tD) = 0.02$, respectively is delayed by the same small time difference as well. In contrast the breakthrough curves for the fractional Brownian motion fields show clear indication of early breakthrough (all 10 breakthrough curves reach $pD = 0.95$ earlier than the uniform case, on average, by $\log_{10}(\Delta tD) = 0.25$) and late-time tailing (7 out of the 10 breakthrough reach $pD = 0.05$ later than the uniform case, on average by $\log_{10}(\Delta tD) = 0.51$). Hence it is very likely that diffusion is anomalous in these particular random fields generated and therefore pressure diffusion through them should not be modelled with the mean hydraulic diffusivity of the random field.

5 Results

5.1 General Observations

The key observations, using the approach depicted in Figure 10 to analyse the occurrence of early breakthrough and late-time tailing in the breakthrough curves are presented in Table 1 (for 2D fields generated with fractional Brownian motion), Table 2 (for 2D fields generated with exponential covariance), and Table 3 (for 3D fields generates with exponential covariance). The observation that early breakthrough and late-time tailing is frequently occurring suggests that anomalous pressure diffusion could be possible if the following holds:

1. The random field has sufficient degrees of heterogeneity, either in terms of variance in hydraulic diffusivity $\eta(x)$, large correlation length ℓ (for random fields with exponential covariance) or large $\mathcal{H}$ (for random fields generated with fractional Brownian motion).
2. Early breakthrough and late-time tailing are more likely to occur in 2D random fields generated with fractional Brownian motion, particularly for low variances in $\eta(x)$.
3. Early breakthrough and late-time tailing are more apparent closer to the location where the pressure is perturbed (e.g. near a well). With increasing distance away from the pressure disturbance, the pressure front (i.e. fluid flow) has sampled more of the heterogeneity in the random field and approaches normal diffusion, in agreement with the general understanding that anomalous diffusion becomes normal at late time. However, Early breakthrough and late-time tailing can still occur at large distances away from the pressure disturbance, especially if the variance in $\eta(x)$ is large. There are some instances were Early breakthrough and late-time tailing appear to become even more obvious with increasing distance (e.g. there is no clear tailing at $\xi = 0.25$ for $\log_{10}(\Delta\eta) = 8$ and $\mathcal{H} = 0.5$ but tailing is strongly evident at $\xi = 0.5$ and $\xi = 0.75$).
4. Early breakthrough and late-time tailing are less obvious if diffusion occurs radially towards a single point. Here, only early breakthrough is observed clearly in the 2D simulations at $\rho = 0.75$ for cases where the variance in η is large.

	$\xi = 0.25$	$\xi = 0.5$	$\xi = 0.75$	$\rho = 0.25$	$\rho = 0.5$	$\rho = 0.75$
$\log_{10}(\Delta\eta) = 4$ $\mathcal{H} = 0.25$	E(10,-0.14)	e(10,-0.05)	U	U	U	U
$\log_{10}(\Delta\eta) = 4$ $\mathcal{H} = 0.5$	E(10,-0.17) t(5,0.25)	e(8,-0.08) t(6,0.27)	E(10,-0.11)	T(8,0.20)	t(9,0.09)	U
$\log_{10}(\Delta\eta) = 4$ $\mathcal{H} = 0.75$	E(9,-0.47) t(5,0.43)	E(9,-0.20) T(8,0.29)	E(10,-0.19) T(10,0.18)	T(8,0.12)	t(8,0.09)	t(9,0.06)
$\log_{10}(\Delta\eta) = 8$ $\mathcal{H} = 0.25$	E(10,-0.29)	E(10,-0.14) T(8,0.13)	E(10,-0.18) t(10,0.07)	t*(4,0.31)	t*(5,0.18)	e(10,-0.09) t*(10,0.08)
$\log_{10}(\Delta\eta) = 8$ $\mathcal{H} = 0.5$	E(10,-0.64) t(5,0.49)	E(10,-0.25) T(7,0.51)	E(10,-0.31) T(10,0.34)	t*(6,0.49)	t*(7,0.31)	E(8,-0.13) t*(10,0.24)
$\log_{10}(\Delta\eta) = 8$ $\mathcal{H} = 0.75$	E(9,-1.00) T(9,0.79)	E(10,-0.46) T(10,0.54)	E(10,-0.45) T(10,0.68)	t*(7,0.18)	t*(6,0.22)	t*(10,0.26)
$\log_{10}(\Delta\eta) = 12$ $\mathcal{H} = 0.25$	E(10,-0.45) t(3,0.54)	E(10,-0.22) T(10,0.30)	E(10,-0.20) T(10,0.19)	t*(6,0.46)	t*(7,0.28)	E(9,-0.18) t*(10,0.29)
$\log_{10}(\Delta\eta) = 12$ $\mathcal{H} = 0.5$	E(10,-1.02) T(7,1.06)	E(10,-0.45) T(8,0.99)	E(10,-0.40) T(10,0.64)	t*(7,0.58)	t*(7,0.66)	E(10,-0.29) t*(9,1.76)
$\log_{10}(\Delta\eta) = 12$ $\mathcal{H} = 0.75$	E(10,-0.75) T(8,1.14)	E(10,-0.55) T(10,0.98)	E(10,-0.72) T(10,1.17)	t*(7,0.19)	t*(7,0.52)	E(8,-0.15) t*(9,1.02)

Table 1 (previous page). Analysis of early breakthrough and late-time tailing as indicators for anomalous diffusion for all breakthrough curves recorded in all the 2D random fields that were generated using fractional Brownian motion. $\log_{10}(\Delta\eta)$ indicates the variance in hydraulic diffusivity (e.g. $\log_{10}(\Delta\eta) = 8$ refers to the case where $\log_{10}(\eta) \in [-4, 4]$). Note that breakthrough curves recorded at a given distance ξ are for diffusion from left to right while breakthrough curves recorded at a given radial distance ρ are for radial diffusion away from a central point. E and T indicate clear early breakthrough and/or late-time tailing in that more than 50% of the breakthrough curve show early breakthrough and/or late-time tailing and $\log_{10}(\Delta tD)$ is sufficiently large. We interpret this as strong indication for anomalous diffusion. e and t indicate possible early breakthrough and/or late-time tailing in that more approximately 50% of the breakthrough curve show early breakthrough and/or late-time tailing and $\log_{10}(\Delta tD)$ is comparatively small. t* indicates possible tailing in the radial diffusion simulations but tailing may be exaggerated because the central point is located in a zone with very low hydraulic diffusivity and hence diffusion towards this point is very slow (see discussion below). U denotes that early breakthrough and long tailing are absent and diffusion is uniform, i.e. normal, such that it can readily be modelled with the mean hydraulic diffusivity of the random field. The first number in the parenthesis denotes the number of breakthrough curves showing early breakthrough (EB in Figure 10), respectively late-time tailing (LT in Figure 10), the second number shows the average $\log_{10}(\Delta tD)$ for these curves. Refer to Figure 10 for the analysis of early and late breakthrough from the breakthrough curves.

	$\xi = 0.25$	$\xi = 0.5$	$\xi = 0.75$	$\rho = 0.25$	$\rho = 0.5$	$\rho = 0.75$
$\log_{10}(\Delta\eta) = 4$ $\ell = 0.001$	t(8,0.08)	U	U	t*(7,0.12)	U	U
$\log_{10}(\Delta\eta) = 4$ $\ell = 0.01$	e(10,-0.09)	U	U	U	U	U
$\log_{10}(\Delta\eta) = 4$ $\ell = 0.1$	E(10,-0.21) t(6,0.11)	e(7,-0.10) t(6,0.15)	e(10,-0.10)	t*(5,0.30)	t*(6,0.09)	U
$\log_{10}(\Delta\eta) = 8$ $\ell = 0.001$	E(10,-0.17) t(6,0.16)	e(10,-0.08) t(7,0.07)	e(10,-0.06)	t*(6,0.22)	U	U
$\log_{10}(\Delta\eta) = 8$ $\ell = 0.01$	E(10,-0.29) t(4,0.21)	E(9,-0.15) t(9,0.07)	e(10,-0.09)	t*(5,0.41)	U	U
$\log_{10}(\Delta\eta) = 8$ $\ell = 0.1$	E(9,-0.64) t(5,0.40)	E(10,-0.29) t(6,0.36)	E(10,-0.25) T(10,0.12)	t*(4,0.57)	t*(7,0.19)	e(10,-0.13) t(10,0.09)
$\log_{10}(\Delta\eta) = 12$ $\ell = 0.001$	E(10,-0.35) T(7,0.20)	E(10,-0.18) T(7,0.15)	E(10,-0.14) t(9,0.05)	t*(7,0.34)	e(6,-0.21) t*(7,0.15)	e(9,-0.10)
$\log_{10}(\Delta\eta) = 12$ $\ell = 0.01$	E(10,-0.52) T(8,0.27)	E(10,-0.28) T(8,0.14)	E(10,-0.19) t(10,0.08)	t*(5,0.67)	e(5,-0.16) t(6,0.11)	e(10,-0.09)
$\log_{10}(\Delta\eta) = 12$ $\ell = 0.1$	E(8,-0.92) t(5,0.65)	E(10,-0.40) T(8,0.61)	E(10,-0.43) T(10,0.40)	t*(6,0.59)	t*(7,0.50)	E(10,-0.22) t(10,0.22)

Table 2. Analysis of early breakthrough and late-time tailing for all breakthrough curves recorded in all the 2D random fields that were generated for an exponential covariance. Refer to Figure 10 for the analysis of early and late breakthrough from the breakthrough curves and Table 1 for the definitions of E, T, e, t, and t* as well as the numbers in the parenthesis.

	$\xi = 0.25$	$\xi = 0.5$	$\xi = 0.75$	$\rho = 0.25$	$\rho = 0.5$	$\rho = 0.75$
$\log_{10}(\Delta\eta) = 4$ $\ell = 0.01$	U	U	U	e(8,-0.53)	U	U
$\log_{10}(\Delta\eta) = 4$ $\ell = 0.1$	E(10,-0.13)	e(9,-0.07)	e(10,-0.05)	e(5,-0.53)	e(6,-0.16)	U
$\log_{10}(\Delta\eta) = 8$ $\ell = 0.01$	e(10,-0.10) t(6,0.06)	e(9,-0.05)	U	e(6,-0.58) t*(6,0.09)	e(6,-0.28)	U
$\log_{10}(\Delta\eta) = 8$ $\ell = 0.1$	E(10,-0.45) t(6,0.10)	E(9,-0.23) t(7,0.15)	E(10,-0.17) t(10,0.08)	e(4,-0.57) t*(5,0.12)	e(6,-0.21)	U
$\log_{10}(\Delta\eta) = 12$ $\ell = 0.01$	E(10,-0.23) t(6,0.08)	e(9,-0.10) t(7,0.06)	e(10,-0.07)	e(6,-0.52) t*(6,0.18)	e(6,-0.33)	U
$\log_{10}(\Delta\eta) = 12$ $\ell = 0.1$	E(10,-0.77) T(8,0.27)	E(10,-0.38) T(10,0.31)	E(10,-0.33) T(10,0.25)	e(4,-0.34) t*(6,0.22)	e(6,-0.19) t*(6,0.08)	t*(6,0.06)

Table 3. Analysis of early breakthrough and late-time tailing for all breakthrough curves recorded in all the 3D random fields that were generated for an exponential covariance on a grid of $100 \times 100 \times 100$. Refer to Figure 10 for the analysis of early and late breakthrough from the breakthrough curves and Table 1 for the definitions of E, T, e, t, and t* as well as the numbers in the parenthesis.

5.2 Examples of Pressure Evolution

In this section, selected but representative examples are shown that depict the pressure evolution in the random fields at different times. These examples serve to explain the nature of early breakthrough and late-time tailing and hence the possible origin of anomalous pressure diffusion. They also highlight why late-time tailing may be overestimated in the radial diffusion simulations.

5.2.1 Fractional Brownian Motion with $\log_{10}(\eta) \in [-2, 2], \mathcal{H} = 0.25$

Early breakthrough is observed in these random fields for simulations where the pressure front travels from left to right through the random field (Figure 11). Early breakthrough is caused by areas where the hydraulic diffusivity is higher (up to two orders of magnitude) than the mean hydraulic diffusivity of $\log_{10}(\eta) = 0$. The pressure front advances faster in these areas and hence pD declines at a faster rate compared to the prediction of pD in a model that assume a uniform hydraulic diffusivity (Figure 12). As a result, a large "island", measuring approximately 25% of the entire model domain, emerges where pD is lower than pD expected from a model that assumes a uniform average hydraulic diffusivity. This low-pressure area is clearly observable until $tD{\sim}0.5$ but the difference between pD and pD_{uniform}, i.e. the pressure predict for a uniform model with $\log_{10}(\eta) = 0$, vanishes once the pressure front has reached the right model boundary and $tD{\sim}1$.
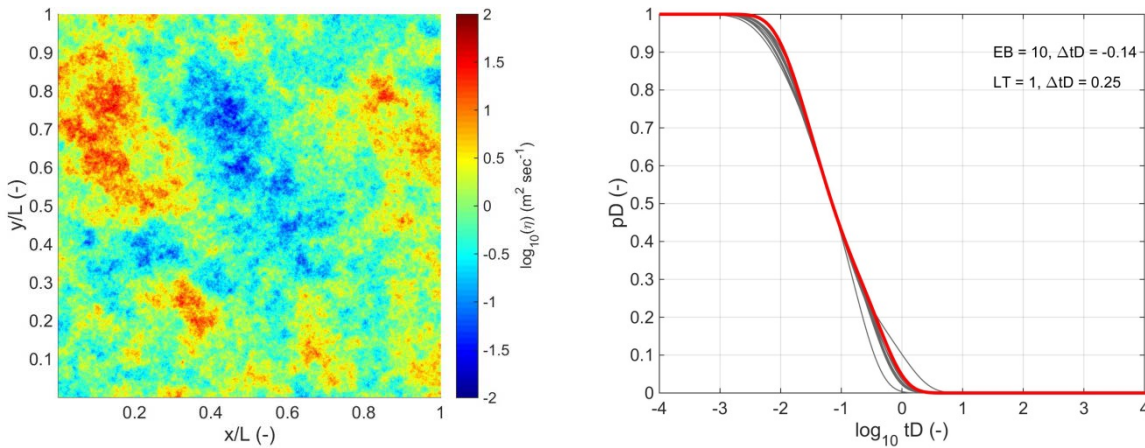

Figure 11. Example of a fractional Brownian motion random field with $\log_{10}(\eta) \in [-2, 2], \mathcal{H} = 0.25$ and shifted breakthrough curves at $\xi = 0.25$ for the left-to-right diffusion case.
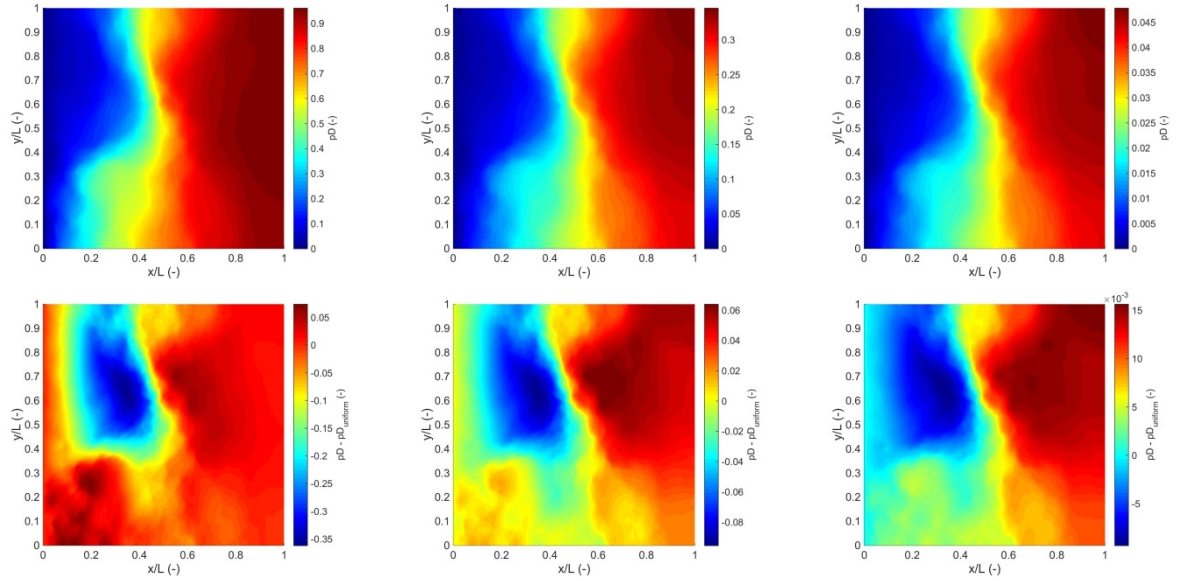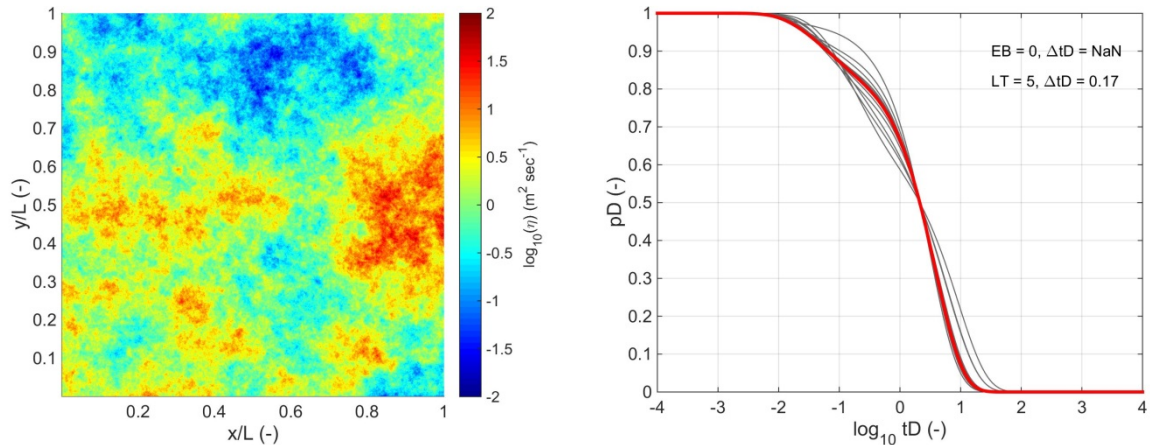
Figure 12. Evolution of pD (top row) and the difference between pD in the random field and pD_{uniform} in a model with uniform hydraulic diffusivity of $\log_{10}(\eta) = 0$ (bottom row) at three different times $tD = 0.1, 0.62,$ and 1.62 (from left to right). Note the different scales. Simulations are for left-to-right diffusion using the random field shown in Figure 11.

In contrast, simulations that use the same field but model pressure diffusion radially away from a single point show no obvious breakthrough and the breakthrough curves (Figure 13). We conjecture that this is because of the radially divergent flow where more of the heterogeneity has been sampled. However, the variations in hydraulic diffusivity lead, like in the left-to-right diffusion case, to large areas where pD decreases faster than what would be expected from a model that has a uniform $\log_{10}(\eta) = 0$. Hence large islands emerge where pD is significantly lower than pD_{uniform} (Figure 14).

Figure 13. Example of a fractional Brownian motion random field with $\log_{10}(\eta) \in [-2, 2], \mathcal{H} = 0.25$ and shifted breakthrough curves at $\rho = 0.25$ for the radial diffusion case.
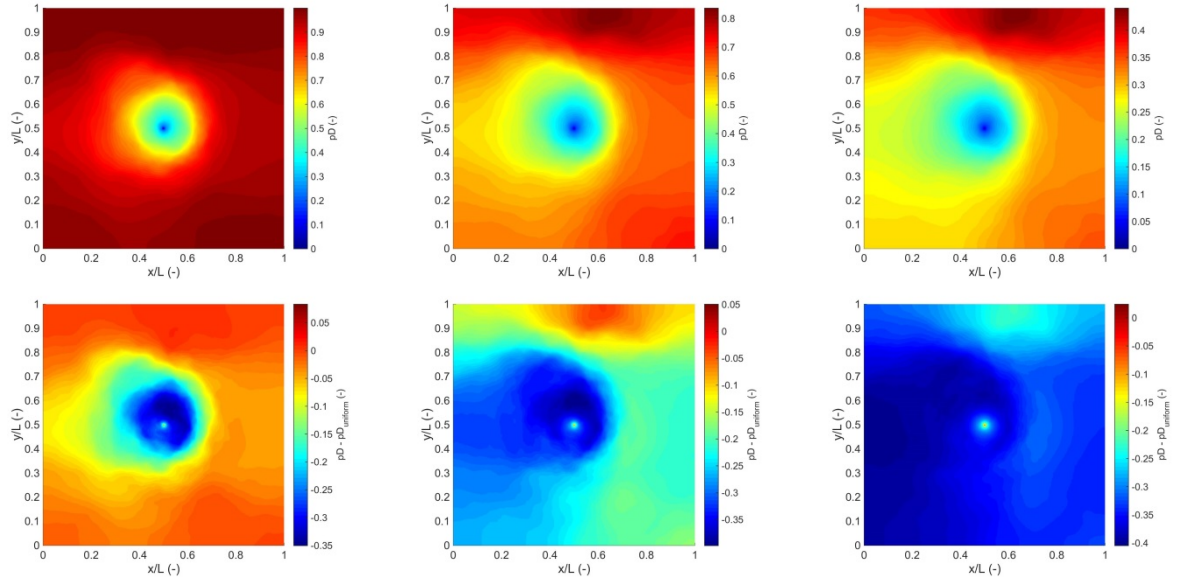
15

Figure 14. Evolution of pD (top row) and the difference between pD in the random field and pD_{uniform} in a model with uniform hydraulic diffusivity of $\log_{10}(\eta) = 0$ (bottom row) at three different times $tD = 0.1, 0.65,$ and 1.7 (from left to right). Note the different scales. Simulations are for radial diffusion using the random field shown in Figure 13.

5.2.2 Fractional Brownian Motion with $\log_{10}(\eta) \in [-6, 6], \mathcal{H} = 0.5$

To contrast the results from Section 5.2.1, we now show results for a random field with extreme heterogeneity. The breakthrough curves for the left-to-right-diffusion case show clear indications of early breakthrough and tailing, even at $\xi = 0.75$, that is far away from the pressure disturbance (Figure 15). As in Section 5.2.1, early breakthrough is due to fast pressure diffusion in areas where hydraulic diffusivity is higher than average. This causes regions where pD decreases faster than what would be expected from a model that has a uniform $\log_{10}(\eta) = 0$. In addition, the areas with low hydraulic diffusivity create islands where pD is significantly higher than pD_{uniform}. These areas cause the late-time tailing in the breakthrough curve as the pressure decreases only slowly in them. Due to the low hydraulic diffusivity in this random field, and large areas where hydraulic diffusivity is low as $\mathcal{H} = 0.5$, these islands of high pressure persists until $tD \gg 1$ (Figure 16). These areas, together with the areas where pD decreases more rapidly than expected, cause the pressure evolution deviates significantly, and for long times, compared to what would be expected from a model that has a uniform $\log_{10}(\eta) = 0$. Combined with the early breakthrough at late-time tailing, the heterogeneous pressure evolution comprise strong evidence that pressure diffusion is anomalous in these random fields.
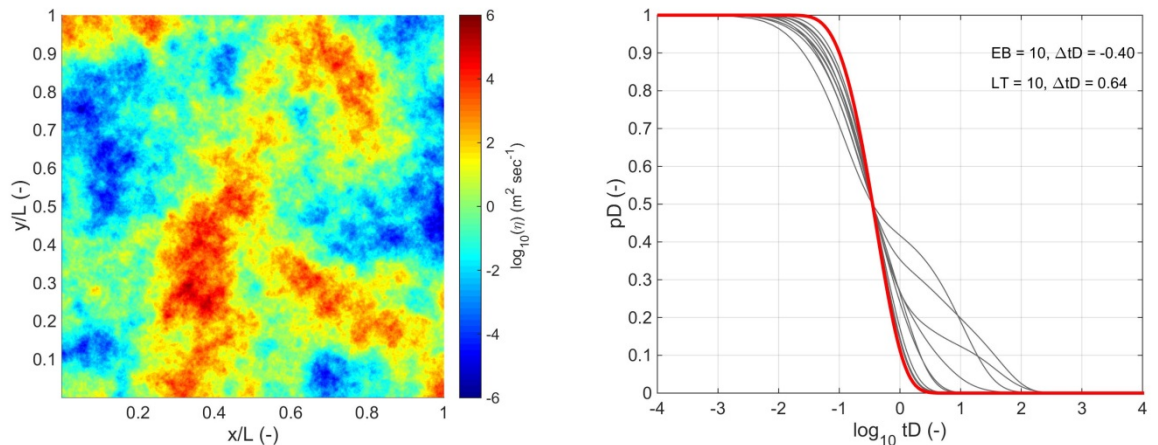

16

Figure 15. Example of a fractional Brownian motion random field with $\log_{10}(\eta) \in [-6, 6], \mathcal{H} = 0.5$ and shifted breakthrough curves at $\xi = 0.75$ for the left-to-right diffusion case.
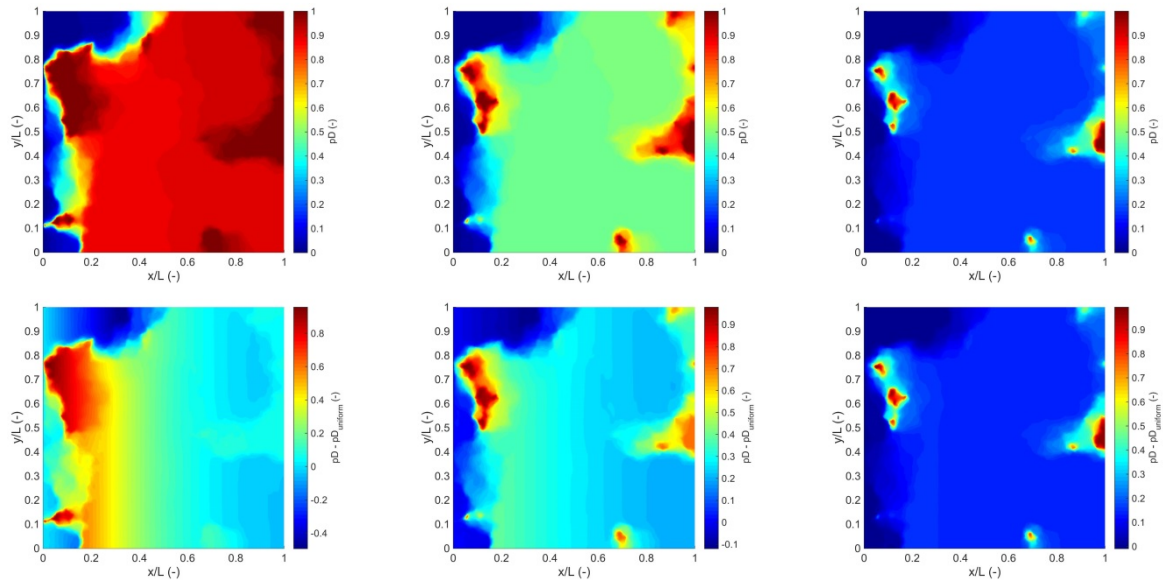

Figure 16. Evolution of pD (top row) and the difference between pD in the random field and pD_{uniform} in a model with uniform hydraulic diffusivity of $\log_{10}(\eta) = 0$ (bottom row) at three different times $tD = 0.1, 0.62,$ and 1.62 (from left to right). Note the different scales. Simulations are for left-to-right diffusion using the random field shown in Figure 15.

Early breakthrough appears to be present in the radial diffusion case for these random fields as well (Figure 17) and, as in the left-to-right diffusion case, pD decreases much faster in regions with high hydraulic diffusivity but remains high and above pD_{uniform} in regions with low hydraulic diffusivity until $tD \gg 1$ (Figure 18). These are strong evidence for anomalous diffusion. Although late-time tailing is also apparent in Figure 17, tailing in some random field is caused if the centre point, where the pressure is perturbed, is located in a region with very low hydraulic permeability (Figure 19). In this case, pressure diffuses radially outwards are a very slow rate, leading to significantly later breakthrough in the un-shifted breakthrough curves (Figure 19 and Figure 20) but breakthrough curves in these cases appear to be parallel to the breakthrough curve with uniform hydraulic diffusivity of $\log_{10}(\eta) = 0$. Anomalous diffusion may be absent in these cases. We also note that such situations are unrealistic from a production point of view, as wells would not be drilled and completed parts of a reservoir where permeability and hydraulic diffusivity are very low. Hence we denoted this kind of late-time tailing as t* in Table 1, Table 2, and Table 3 above.
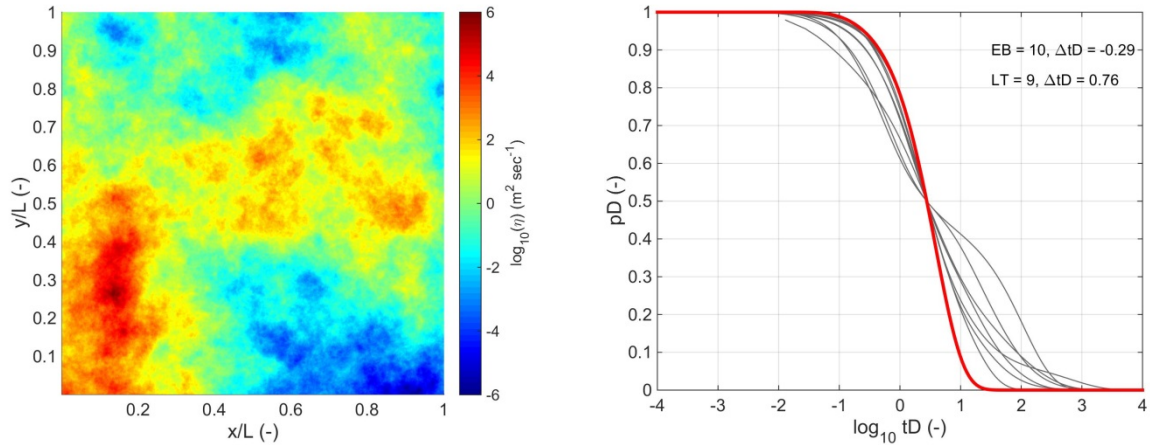
Figure 17. Example of a fractional Brownian motion random field with $\log_{10}(\eta) \in [-6, 6], \mathcal{H} = 0.5$ and shifted breakthrough curves at $\rho = 0.75$ for the radial diffusion case.
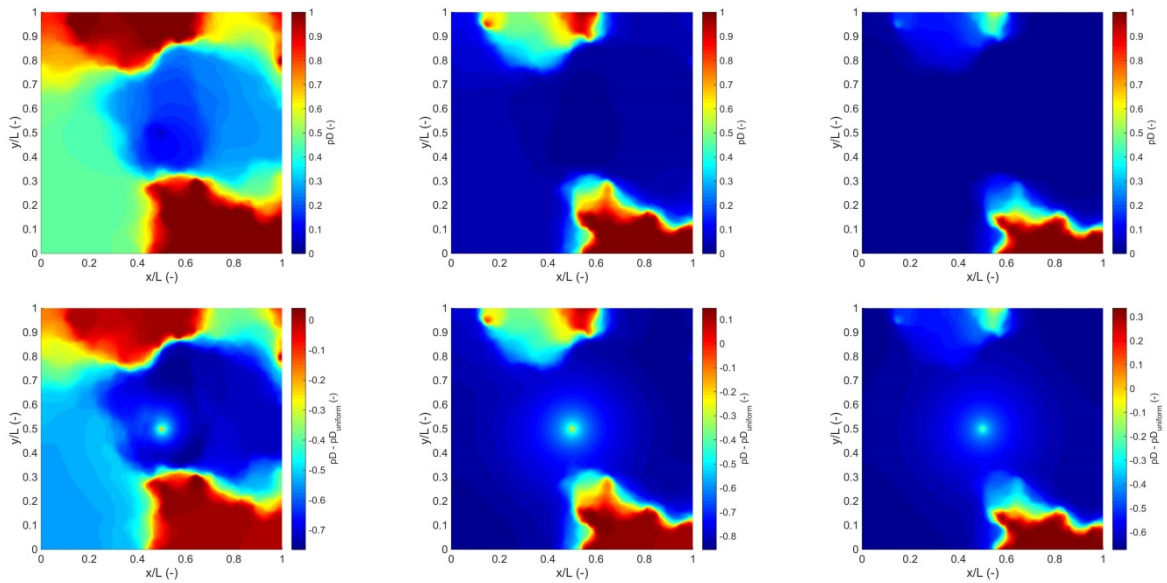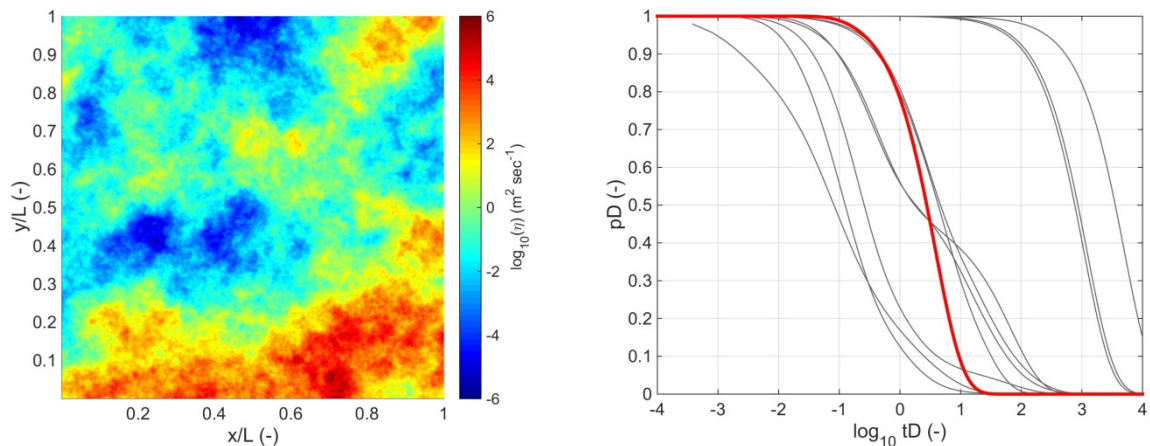

Figure 18. Evolution of pD (top row) and the difference between pD in the random field and pD_{uniform} in a model with uniform hydraulic diffusivity of $\log_{10}(\eta) = 0$ (bottom row) at three different times $tD = 0.1, 0.65,$ and 1.7 (from left to right). Note the different scales. Simulations are for radial diffusion using the random field shown in Figure 17.

Figure 19. Example of a fractional Brownian motion random field with $\log_{10}(\eta) \in [-6, 6], \mathcal{H} = 0.5$ and un-shifted breakthrough curves at $\rho = 0.75$ for the radial diffusion case. Note that in the centre point where the pressure drop is applied is located in a region with very low hydraulic diffusivity. Hence pressure will diffuse radially outwards very slowly, causing the significantly later breakthrough, and apparent late-time tailing in Figure 17.
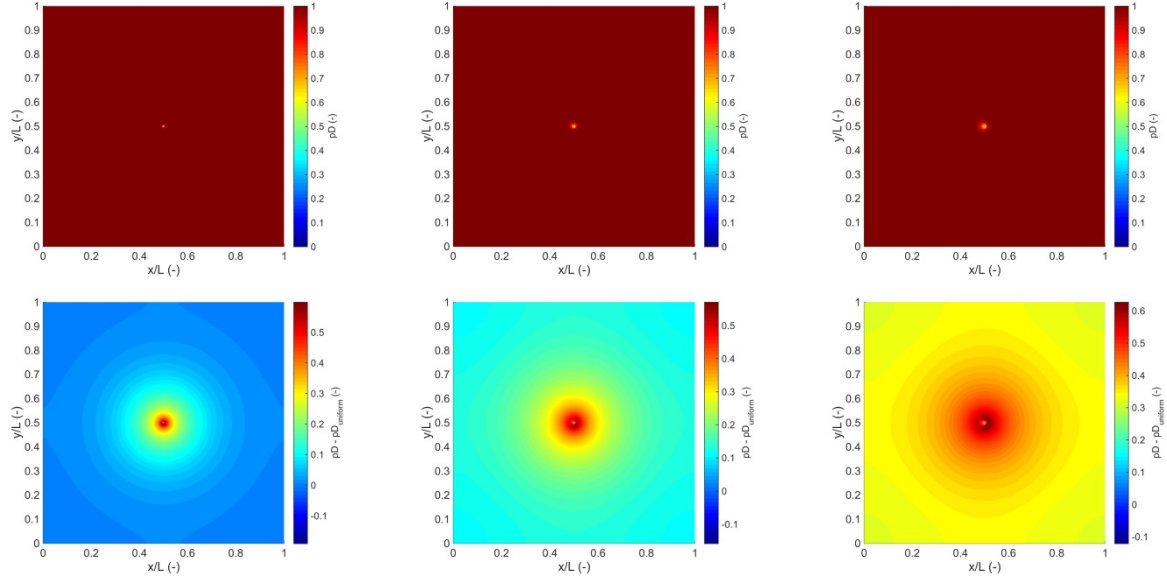
Figure 20. Evolution of pD (top row) and the difference between pD in the random field and pD_{uniform} in a model with uniform hydraulic diffusivity of $\log_{10}(\eta) = 0$ (bottom row) at three different times $tD = 0.1, 0.65,$ and 1.7 (from left to right). Note how slow the pressure diffuses radially outwards because the centre point where the pressure drop is applied is located in a region with very low hydraulic diffusivity. Simulations are for radial diffusion using the random field shown in Figure 19.

5.2.3 2D Exponential Covariance with $\log_{10}(\eta) \in [-4, 4], \ell = 0.01$

As an example with intermediate heterogeneity, we present results for random fields with an exponential covariance and $\log_{10}(\eta) \in [-4,4], \ell = 0.01$. Breakthrough curves for the left-to-right diffusion in these fields show some indication of early breakthrough and tailing in the left-to-right and radial diffusion cases (Figure 21 and Figure 23), but significantly less compared to the breakthrough curves discussed in Section 5.2.2. If these breakthrough curves were to exhibit anomalous diffusion could only be quantified rigorously using a CTRW analysis. However, maps showing the evolution in pD in comparison to pD_{uniform} show distinct areas where the pressure declines faster or stays compared to what would be expected from a model with uniform hydraulic diffusivity of $\log_{10}(\eta) = 0$, both for the left-to-right (Figure 20) and radial diffusion case (Figure 22). Due to the comparatively short correlation length and the exponential rate at which hydraulic diffusivity changed from low to high values, the regions where pD deviates from pD_{uniform} are small and these deviations are short-lived compared to the more heterogeneous random fields discussed above. Hence less late-time tailing and early breakthrough is observed.
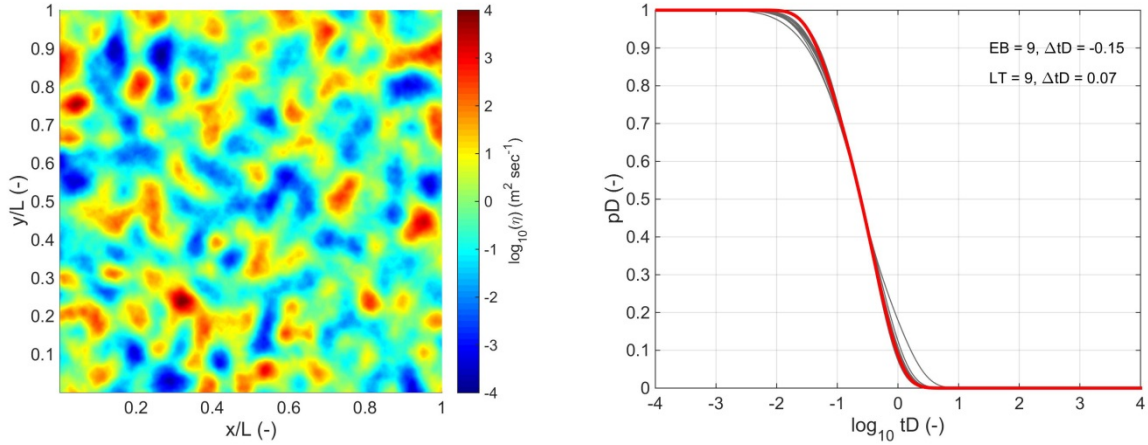
Figure 21. Example of a 2D random field with exponential covariance and $\log_{10}(\eta) \in [-4, 4], \ell = 0.01$ and shifted breakthrough curves at $\xi = 0.5$ for the left-to-right diffusion case.
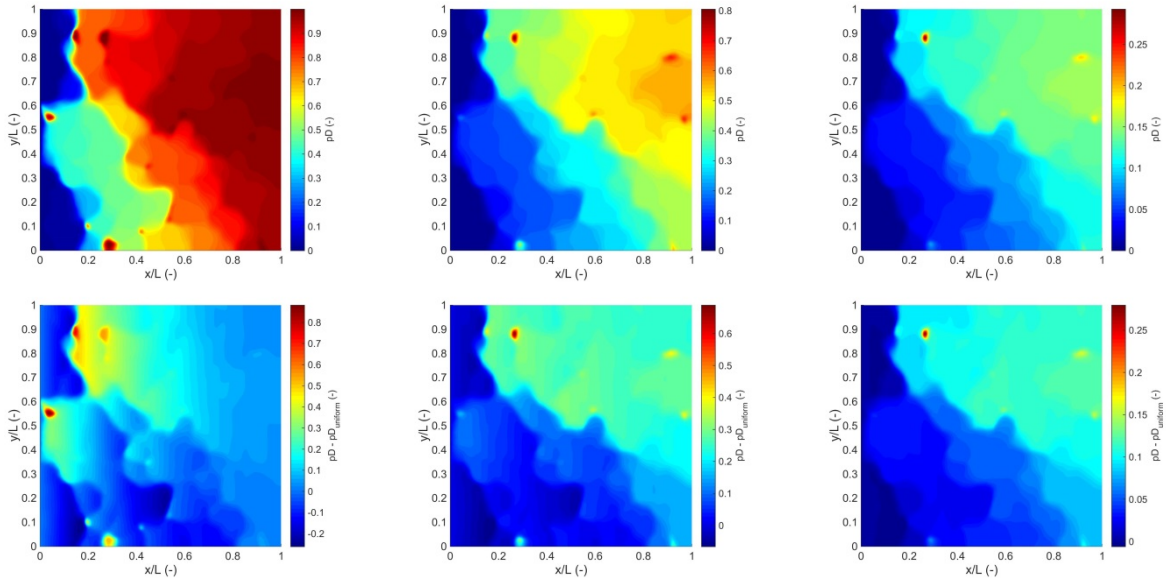

Figure 22. Evolution of pD (top row) and the difference between pD in the random field and pD_{uniform} in a model with uniform hydraulic diffusivity of $\log_{10}(\eta) = 0$ (bottom row) at three different times $tD = 0.1, 0.62,$ and 1.62 (from left to right). Note the different scales. Simulations are for left-to-right diffusion using the random field shown in Figure 21.
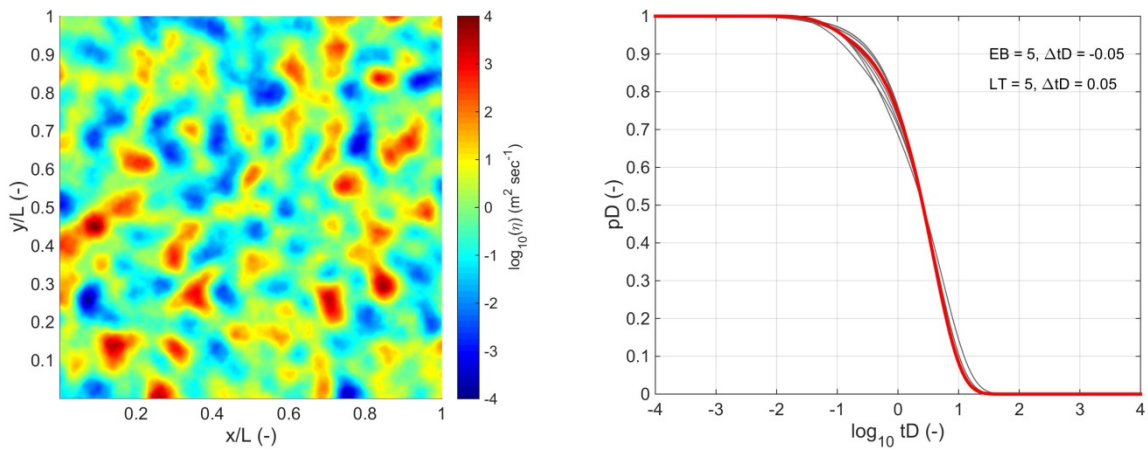

Figure 23. Example of a 2D random field with exponential covariance and $\log_{10}(\eta) \in [-4, 4], \ell = 0.01$ and shifted breakthrough curves at $\rho = 0.5$ for the radial diffusion case.
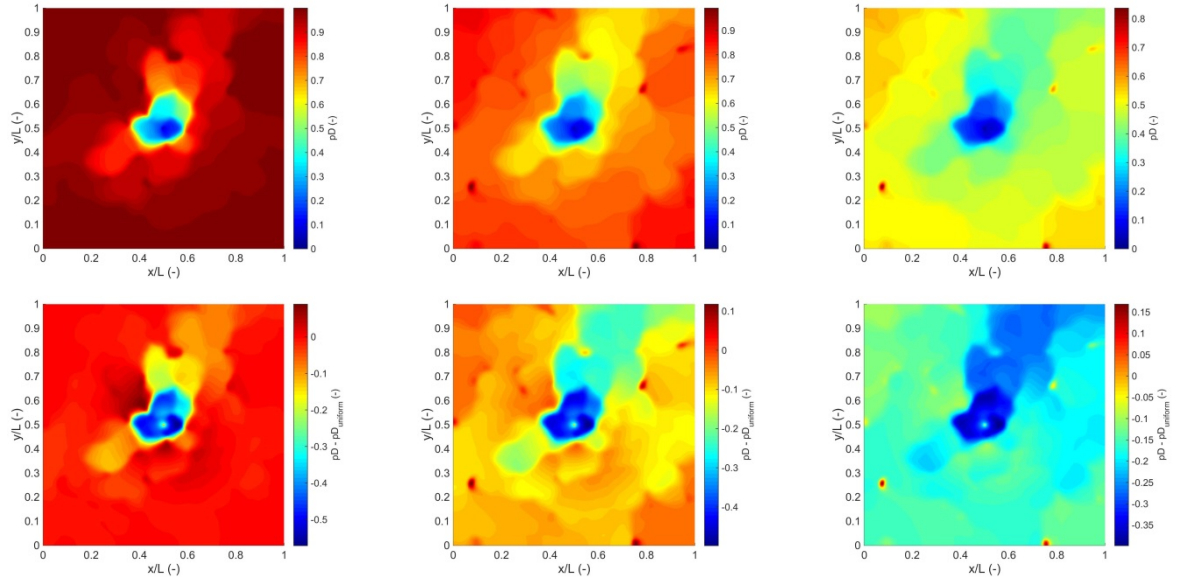
Figure 24 (Previous page). Evolution of pD **(top row) and the difference between** pD **in the random field and** pD_{uniform} **in a model with uniform hydraulic diffusivity of** $\log_{10}(\eta) = 0$ **(bottom row) at three different times** $tD = 0.1, 0.65,$ **and** 1.7 **(from left to right). Note the different scales. Simulations are for radial diffusion using the random field shown in Figure 23.**

5.2.4   3D Exponential Covariance with $\log_{10}(\eta) \in [-4, 4], \ell = 0.1$

This section illustrates that early breakthrough and late-time tailing also occur, and hence anomalous pressure diffusion could be present, in 3D models, given sufficient degrees of heterogeneity (Figure 25). As in the 2D cases discussed above, regions emerge where the pressure advances faster or slower, depending on the hydraulic diffusivity, compared to what would be expected in from a model that has uniform hydraulic diffusivity of $\log_{10}(\eta) = 0$. These deviations are apparent in both, the left-to-right (Figure 26) and radial (Figure 27) diffusion cases. However, as the in the examples above, the breakthrough curves for the radial diffusion case do not show clear evidence for early breakthrough or late-time tailing (Figure 27).
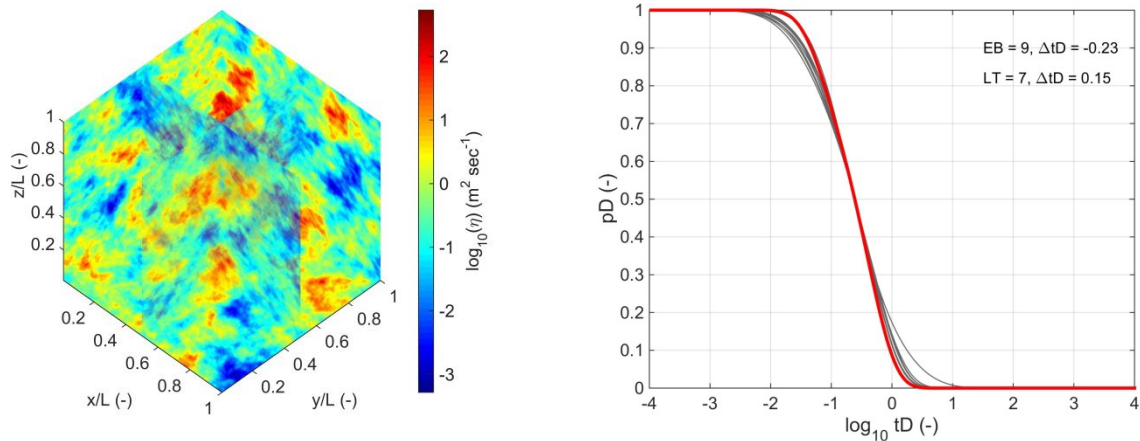

Figure 25. Example of a 3D random field with exponential covariance and $\log_{10}(\eta) \in [-4, 4], \ell = 0.1$ **and shifted breakthrough curves at** $\xi = 0.5$ **for the left-to-right diffusion case.**
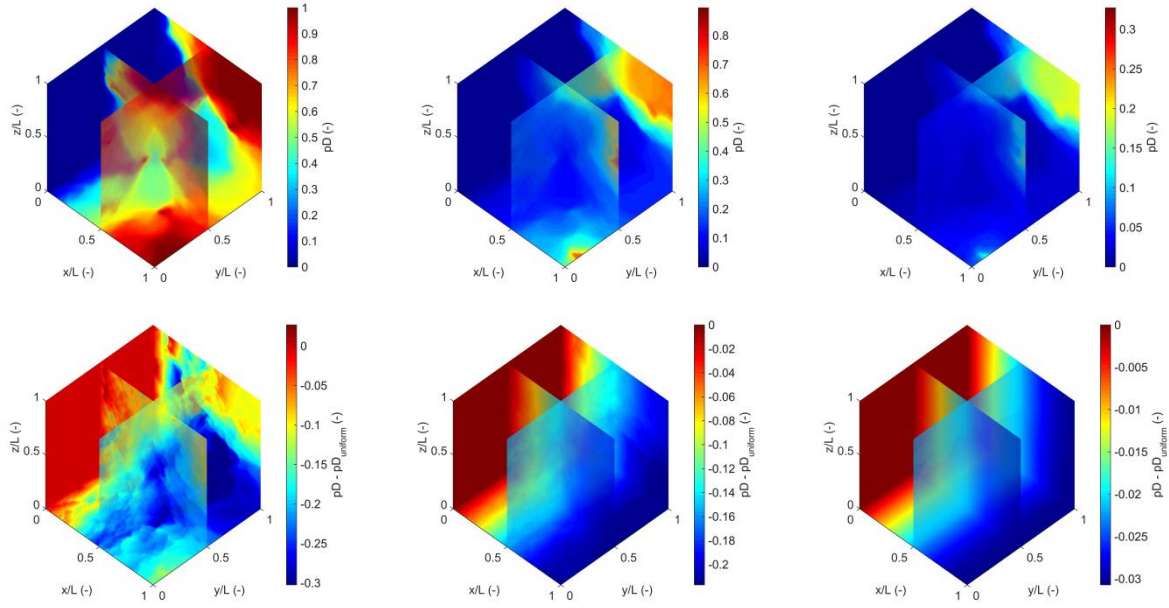
Figure 26. Evolution of pD (top row) and the difference between pD in the random field and $pD_{uniform}$ in a model with uniform hydraulic diffusivity of $\log_{10}(\eta) = 0$ (bottom row) at three different times $tD = 0.1, 0.62,$ and 1.62 (from left to right). Note the different scales. Simulations are for left-to-right diffusion using the random field shown in Figure 25.
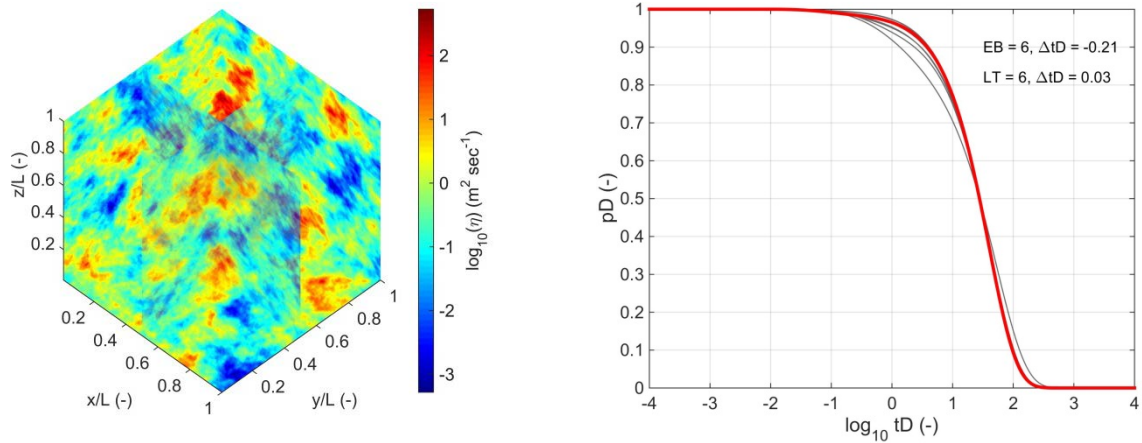

Figure 27. Example of a 2D random field with exponential covariance and $\log_{10}(\eta) \in [-4, 4], \ell = 0.1$ and shifted breakthrough curves at $\rho = 0.5$ for the radial diffusion case.
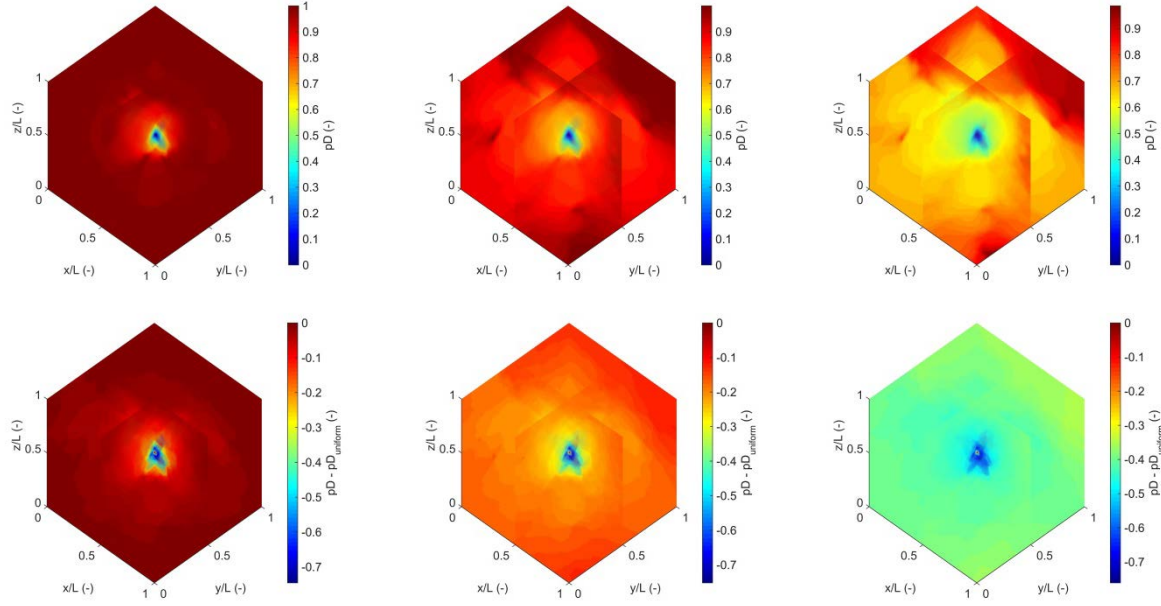
Figure 28. Evolution of pD (top row) and the difference between pD in the random field and pD_{uniform} in a model with uniform hydraulic diffusivity of $\log_{10}(\eta) = 0$ (bottom row) at three different times $tD = 0.1, 0.65,$ and 1.7 (from left to right). Note the different scales. Simulations are for radial diffusion using the random field shown in Figure 27.

5.2.5 Impact of Grid Refinement in 3D

To test the impact on grid refinement on anomalous diffusion in 3D, we generated random fields using the same parameters, i.e. with $\ell = 0.1$ and 0.001 and variations in $\log_{10}(\eta)$ between $[-2,2]$, $[-4,4]$ and $[-6,6]$ on a grid of $200 \times 200 \times 200$. Although changes in the shape of the breakthrough curves are visible for grids of $100 \times 100 \times 100$ and $200 \times 200 \times 200$ (Figure 29), the statistical analysis of the breakthrough curves shows that additional grid refinement has negligible impact on anomalous diffusion in 3D (Table 4) when compared to the statistical analysis of the simulation results for a grid of $100 \times 100 \times 100$ (Table 3). The variations in early breakthrough and late tailing can probably be explained by the differences in the random fields, which were created using different seeds (but the same parameters) for both levels of grid refinement.

	$\xi = 0.25$	$\xi = 0.5$	$\xi = 0.75$	$\rho = 0.25$	$\rho = 0.5$	$\rho = 0.75$
$\log_{10}(\Delta\eta) = 4$ $\ell = 0.01$	U	U	U	e(8,-0.29)	U	U
$\log_{10}(\Delta\eta) = 4$ $\ell = 0.1$	e(9,-0.11) t(7,0.10)	e(10,-0.06) t(6,0.05)	e(10,-0.05)	e(5,-0.55)	e(5,-0.09)	U
$\log_{10}(\Delta\eta) = 8$ $\ell = 0.01$	e(10,-0.08)	U	U	e(7,-0.69)	e(7,-0.11)	U
$\log_{10}(\Delta\eta) = 8$ $\ell = 0.1$	E(10,-0.36) T(7,0.16)	E(10,-0.20) t(6,0.14)	E(10,-0.18) t(10,0.06)	e(4,-0.66) t*(6,0.11)	e(5,-0.16)	U
$\log_{10}(\Delta\eta) = 12$ $\ell = 0.01$	E(10,-0.20)	e(9,-0.10)	e(10,-0.06)	e(7,-0.80)	e(7,-0.16)	U
$\log_{10}(\Delta\eta) = 12$ $\ell = 0.1$	E(9,-0.54) T(8,0.39)	E(10,-0.35) T(10,0.31)	E(10,-0.31) T(10,0.20)	e(6,-0.53) t*(6,0.32)	e(6,-0.27) t*(7,0.10)	e(7,-0.07)

Table 4. Analysis of early breakthrough and late-time tailing for all breakthrough curves recorded in all the 3D random fields and a grid of $200 \times 200 \times 200$ that were generated for an exponential covariance. Refer to Figure 10 for the analysis of early and late breakthrough from the breakthrough curves and Table 1 for the definitions of E, T, e, t, and t* as well as the numbers in the parenthesis. See Table 3 for comparison with a grid of $100 \times 100 \times 100$.
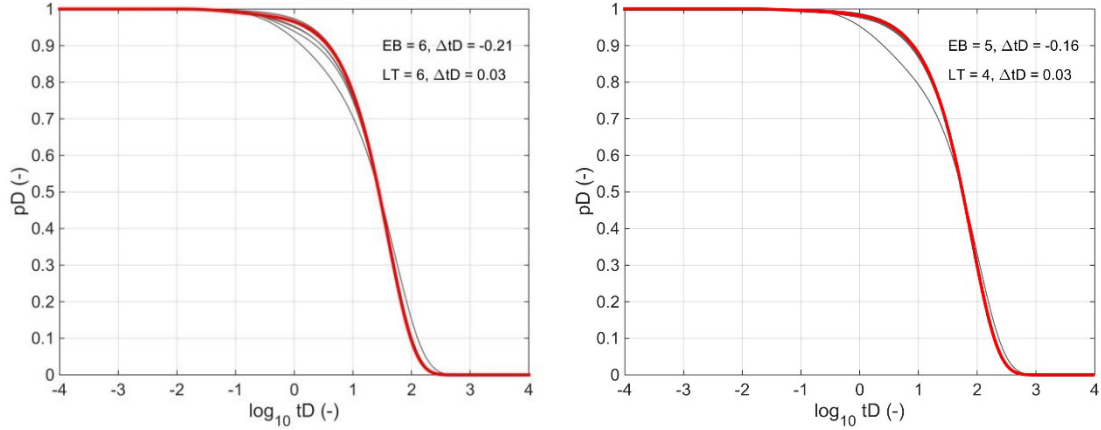
Figure 29. Comparison of the shifted breakthrough curve for the radial diffusion case at $\rho = 0.5$ with $\log_{10}(\eta) \in [-4, 4]$, $\ell = 0.1$ on a grid of $100 \times 100 \times 100$ (left) and $200 \times 200 \times 200$ (right).

6 Concluding Remarks

Results from 360 high-resolution simulations (in 2D) and 240 high-resolution simulations (in 3D) that model pressure diffusion through random fields with different degrees of heterogeneity show that early breakthrough and late-time tailing can be significant if the heterogeneity is large, i.e. if the correlation length of the heterogeneity variations is large and/or the variance in hydraulic diffusivity is large. Early breakthrough and late-time tailing are strong evidence of anomalous diffusion but a unambiguous answer if anomalous diffusion is prevalent is only possible if the breakthrough curves are analysed rigorously and quantitatively using CTRW.

Although breakthrough curves for radial diffusion (i.e. pressure diffusion away from a single point) exhibit less early breakthrough and tailing compared to breakthrough curves where the pressure diffuses from left to right through the model, both diffusion scenarios can lead to regions of significant size in the model where the pressure decreases faster or slower than what would be predicted from a model that assumes a uniform hydraulic diffusivity that is equal to the mean of the random field. Such regions could correspond to areas where the reservoir compacts faster, respectively slower, than what would be expected from a reservoir simulation that uses averaged properties (e.g. permeability) at the scale of a reservoir simulation grid block.

We note that the random fields that have been generated are not using data from a real subsurface reservoir and, as a consequence, some of the random fields have up to 12 orders magnitude in variation in hydraulic diffusivity. While these variations are larger than the permeability variations observed in typical reservoir facies, they may not be unrealistic once the hydraulic diffusivity of non-reservoir facies (e.g. shales, mudstones) is considered. Although the non-reservoir facies may not impact depletion and production directly and may hence be excluded (e.g. in the form of inactive cells) in a reservoir simulation model, they will still be affected by changes in reservoir pressure: Our simulation results show that the pressure decreases noticeably slower in regions of low hydraulic diffusivity while early breakthrough is caused by the regions where hydraulic diffusivity is high.

Hence both cases, early breakthrough and late-time tailing, could explain why reservoir simulation models with average grid block properties may not predict compaction and subsidence at late time adequately. When a simulation model is calibrated to production data such that the onset in

24

variations in bottom-hole pressure (and flow rate) is modelled adequately, the simulation model could predict that compaction and subsidence occurs on average too fast as either the grid-block properties have been increased to capture the early breakthrough or the late-time tailing is neglected in the simulation altogether. On the other hand, if the simulation model excludes regions with non-reservoir facies that have low hydraulic diffusivity, the slow decrease in reservoir pressure in these regions is not captured. Reservoir simulation models that do not represent early breakthrough and/or late-time tailing correctly could therefore fail to model that there are regions in the reservoir, which as our simulations indicate could potentially be large, where the pressure remains high for an extended period. In these regions compaction would always occur at a slower rate than what is predicted by a simulation model with (adjusted) average grid-block property, especially if the size of the simulation grid blocks is large.

7 References

Benson DA, Wheatcraft SW, Merschaert MM, The fractional-order governing equation of Levy motion. Water Resources Research, 36(6), 1413-1423, 2000.

Berkowitz B, Cortis A, Dentz M, Scher H, Modelling non-Fickian transport in geological formations as a continuous time random walk. Reviews of Geophysics, 44, RG2003, 2006

Bijeljic, Blunt MJ, Pore-scale modelling and continuous time random walk analysis of dispersion in porous media. Water Resources Research, 42, W01202, 2006.

Cortis A, Gallo C, Scher H, Berkowitz B, Numerical simulation of non-Fickian transport in geological formations with multiple-scale heterogeneities. Water Resources Research, 40, W04209, 2004.

Cortis A, Berkowitz B, Anomalous transport in classical soil and sand columns. Soil Science Society of America Journal, 68, 1539-1548, 2004.

Cortis A, Berkowitz B, Computing anomalous contaminant transport in porous media: The CTRW Matlab toolbox. Ground Water, 43(6), 947-950, 2005.

Cortis A and Knudby C, A continuous time random walk approach to transient flow in heterogeneous porous media. Water Resources Research, 42, W10201, 2006.

DiDonato G, Obi EO, Blunt MJ, Anomalous transport in heterogeneous media demonstrated by streamline-based simulation. Geophysical Research Letters, 30(12), GL017196, 2003.

Dentz M, Cortis A, Scher H, Berkowitz B, Time behaviour of solute transport in heterogeneous media: Transition from anomalous to normal transport. Advances in Water Resources, 27, 155-173, 2004.

Dietrich CR Newsam GN, Fast and exact simulation of stationary Gaussian processes through circulant embedding of the covariance matrix SIAM Journal of Scientific Computing, 18(4), 1088–1107, 1997.

Geiger S and Emmanuel E, Non-fourier thermal transport in fractured geological media. Water Resources Research, 46, W07504, 2010.

Geiger S, Cortis A, Birkholzer JT, Upscaling solute transport in naturally fractured porous media with the Continuous Time Random Walk Method. Water Resources Research, 46, W12530, doi:10.1029/2010WR009133, 2010.

Gneiting T, Closed form solutions of the two dimensional turning bands equation. Mathematical Geology, 30(4),379-390, 1998.

Haggerty R, Gorelick SM, Multiple-rate mass transfer for modelling diffusion and surface reactions in media with pore-scale heterogeneity. Water Resources Research, 31(10), 2383-2400.

Kroese PD, Botev ZI, Spatial process generation. In: Lectures on Stochastic Geometry, Spatial Statistics and Random Fields, Volume II: Analysis, Modeling and Simulation of Complex Structures. Springer, 2014.

Lord GJ, Powell CE, Shardlow T, An introduction to computational stochastic PDEs. Cambridge University Press, 2014.

Matthäi SK, Geiger S, Roberts SG, Paluzny A, Belayneh M, Burri A, Mezentsev A, Lu H, Coumou D, Driesner T, Heinrich CA, Numerical simulations of multiphase fluid flow in structurally complex reservoirs. Geological Society of London Special Publications, 292, 405-429, 2007

Montoglou A, Wilson JL, The turning bands method for simulation of random fields using line generation by a spectral method. Water Resources Research, 18(5), 1379-1394, 1982.

Stüben K, Solving reservoir simulation equations. 9th International Forum on Reservoir Simulation, Abu Dhabi, United Arab Emirates, 2007.

Rhodes ME, Bijeljic B, Blunt MJ, A rigorous pore-to-field-scale simulation method for single-phase flow based on continuous time random walks. SPE Journal, 14(10, 88-94, 2009.